Understanding the sulfate attack of Portland cement–based materials exposed to applied electric fields: Mineralogical alteration and migration behavior of ionic species

Chen Li [a,b], Zhengwu Jiang [a,*], Rupert J. Myers [c,d], Qing Chen [a], Mengxue Wu [a,e], Jiaqi Li [b], Paulo J. M. Monteiro [b,f]

[a] *Key Laboratory of Advanced Civil Engineering Materials of Ministry of Education, Tongji University, 4800 Cao'an Road, Shanghai, 201804, China*

[b] *Department of Civil and Environmental Engineering, University of California, Berkeley, California, 94720, United States*

[c] *School of Engineering, University of Edinburgh, Edinburgh, EH9 3FB, United Kingdom*

[d] *Current address: Department of Civil and Environmental Engineering, Imperial College London, London, SW7 2AZ, United Kingdom*

[e] *Administration for Market Regulation of Chengdu, Sichuan, 610044, China*

[f] *Material Science Division, Lawrence Berkeley National Laboratory, Berkeley, California, United States*

[*] Corresponding author

E-mail address: jzhw@tongji.edu.cn (Z. Jiang).

Abstract

The magnesium and sodium sulfate attacks on Portland cement paste in the presence of applied electric fields were studied, and the mineralogical alterations were investigated by both experiments and thermodynamic modeling. When an electric current flows out of the cement paste, the electric migration of ions induced sulfate ingress and decalcification. Compared with the specimen exposed to Na_2SO_4, that exposed to $MgSO_4$ for 28 d proceeded to a later degradation stage, which is characterized by the decomposition of ettringite, portlandite, and AFm phases, and the formation of $CaSO_4$. Thermodynamic modeling indicates a neutralization process induced by the electric migration of OH^-, which is potentially responsible for the decomposition of ettringite. When an electric current flows into the cement paste, the Mg^{2+} and Na^+ showed different migration behavior. Mg^{2+} was incorporated to form brucite and M-S-H–like products in a shallow area (~100 μm) on the surface of the specimen, whilst a part of the Na^+ could be bonded to form Na-rich silica gel with the other part penetrating through the specimen. By coupling the pore solution chemistry obtained from thermodynamic modeling with the Nernst-Planck equation, the migration behaviors of the ionic species (SO_4^{2-}, Mg^{2+}, and Na^+) were analyzed.

Keywords

Sulfate attack; Mineralogical alteration; Thermodynamic modeling; Nernst-Planck equation; Applied electric field

1 Introduction

Cement-based materials are porous and consist of multiple phases. The hydration products (solid phase) form the

38   skeleton of the pore structures, and the pore solution (aqueous phase) and air (gaseous phase) fill inside the pores.

39   In a fully hydrated cement paste, the hydration products are approximately at equilibrium with the pore solution.

40   However, this state will be affected by the ionic exchange between the pore solution and the external environment.

41   Such a process usually induces mineralogical alterations and is described as a chemical attack. The attack is

42   affected by the type, rate, and direction of the ion exchange, as well as the chemical reactions that occur.

43

44   The ingress of external sulfate will cause sulfate attack, which is one of the most widely recognized and

45   well-studied chemical attacks. In Portland cement systems, sulfate attacks are usually characterized by the

46   formation of ettringite, and by the expansion, cracking, and strength loss thereafter [1-3]. Recent theories relate the

47   expansion to the crystallization pressure caused by the formation of ettringite from oversaturated solution in small

48   pores [4-6]. The crystals growing in confined pores, e.g., in the C-S-H gel, generate crystallization pressure and

49   thus expansive stress [7,8], whilst those growing in unrestrained pore spaces do not. Gypsum usually forms at the

50   late stage of sulfate attack. There was once a debate on whether the formation of gypsum is a cause [9-11] or an

51   effect [12,13] of the expansion and cracking. Recent studies proposed that the presence of gypsum induces a high

52   supersaturation with respect to ettringite, and thus a high crystallization pressure and more expansion [2,14,15].

53

54   The type of cation that coincides with sulfate greatly influences the degradation process. When the cation is Mg^{2+},

55   surface erosion occurs in addition to expansion [15-17]. This phenomenon is induced by the formation of brucite

56   and magnesium silicate hydrate (M-S-H) [2,16], and is the most important characteristic to distinguish magnesium

57   sulfate attack from sodium sulfate attack. It was also reported that the co-existence of Na^+, K^+, and Ca^{2+} can reduce

58   surface erosion and expansion in the $MgSO_4$ attack [2,16]. When the sulfate is provided by an acidic environment,

59   neutralization can take place in the pore solution, and the Ca^{2+} can diffuse towards the external environment due to

60   the concentration gradient. Under this circumstance, calcium leaching or decalcification will also occur together

61   with the sulfate attack [18-20].

62

63   In most cases, the ionic exchange between cement-based materials and the external environment is driven by the

64   concentration gradient, and this process is known as diffusion. In certain field conditions, the exposed surface of a

65   structure is subjected to strong evaporation conditions. The moisture gradient between the external environment

66   and cement-based materials induces capillary suction, and the ionic species will be transported by advection [21].

67   Under an applied electric field, the ionic species in the pore solution can also migrate, which is known as electric

68   migration [22-24]. The transportation of ionic species—their diffusion, advection, and electric migration in

69   cement-based materials is described by the Nernst-Planck equation [22-25]. During the ionic transportation,

70   chemical reactions can take place. For example, SO_4^{2-} can react with monosulfate to form ettringite [1,20,26]. This

71   reaction impacts not only the mass transport of SO_4^{2-} but also the strength of Ca^{2+} and AlO_2^- by disturbing the

72   equilibrium between the hydration products and the pore solution. In this respect, the concurrent chemical reactions

73   and ionic transportation both play significant roles in the ingress of sulfate.

74

75   In some cases, cement-based materials are directly exposed to applied electric fields, e.g., the DC stray current that

76   is present in underground metro tunnels [27-29]. Electric migration can accelerate the ingress of aggressive ions

77   from the external environment and remove the calcium and alkali metals from the pore solution [30,31]. Electric

78   fields are also applied in some modern concrete techniques, e.g., chloride extraction, realkalinization, cathodic

79   protection, and electrochemical deposit [32-35]. In these techniques, certain types of ions are designed to migrate,

80   but the migrations of other ions have to be considered because they may induce side effects [36]. Electric migration

81   is also a useful tool for laboratory acceleration tests, e.g., the chloride ion penetration tests (ASTM C1202), calcium

82   leaching acceleration tests [37,38], etc. Recent studies proposed that electric migration tests can be potentially used

83   in the acceleration of sulfate attacks [39-41]. However, a deeper understanding of the mineralogical alterations and

84   the degradation mechanism under such circumstances will be needed to evaluate the validity of this technique.

85

86   In a conventional sulfate attack caused by diffusion, both the cations and anions in the external solution diffuse into

87   the cement-based materials, while the ions in the pore solution, e.g. Ca^{2+}, OH^-, and alkali metal ions diffuse

88   outward. In contrast, under applied electric fields, the cations and anions migrate in different directions, and thus

89   the degradation behavior and mechanism may differ from the diffusion-induced sulfate attacks. This paper studies

90   the $MgSO_4$ and Na_2SO_4 attacks on Portland cement paste in the presence of applied electric fields. The chemical

91   and mineralogical alterations during the degradation process were analyzed by scanning electron microscopy

92   (SEM), energy dispersive X-ray spectrometry (EDS), X-ray diffractometry (XRD), and thermogravimetric analysis

93   (TGA). The results suggest different degradation behaviors between the areas near the cathode and anode, and

94   between the specimens exposed to different sulfate sources. To better understand the degradation mechanism, an

95   approach was proposed to simplify the electric migration processes, and changes of the phase assemblages during

96   the simplified electric migration processes were then calculated by thermodynamic modeling. By combining the

97   pore solution chemistry obtained in the thermodynamic modeling with the Nernst-Planck equation, the migration

98   behaviors of various ionic species were analyzed to explain the different degradation behaviors observed

99   experimentally.

100

101   **2 Experimental**

102   *2.1 Cement paste specimens*

103

104   Cement paste specimens were prepared using Portland cement and deionized water at a water-to-cement ratio of 0.5.

105   The chemical composition of the Portland cement was tested by X-ray fluorescence spectrometry (XRF), and the

106   mineralogical composition was measured by XRD and analyzed by Rietveld refinement, as shown in Table 1. The

107   specimens were cast into cylindrical molds that were 100 mm in diameter and 50 mm in height, cured at 20 °C ±

108   1 °C, RH > 95% and unmolded after 24 h. The top of the cylinders, which was not in contact with the molds, was

109   polished by P240 (58 μm) sandpaper to make it flat and smooth. The specimens were then cured in saturated

110   limewater at 20 °C ± 1 °C until 28 d.

111

112   **Table 1** Chemical and mineralogical compositions of the Portland cement (wt. %).

| Chemical composition		Mineralogical composition	
Na_2O	0.04	C_3S	58.32
MgO	0.76	C_2S	11.64
Al_2O_3	4.55	C_3A	3.96
SiO	20.8	C_4AF	8.03
P_2O_5	0.11	Calcite	4.58
SO_3	2.92	Anhydrite	0.76
K_2O	0.74	Bassanite	3.67
CaO	64.8	Gypsum	0.01
TiO_2	0.23	Lime	0.35
Cr_2O_3	0.02	Portlandite	0.58
MnO	0.11	CF_2	1.53
Fe_2O_3	3.27	Goergeyite	3.30
CuO	0.02	Perovskite	1.79
ZnO	0.05	Periclase	0.85
SrO	0.03	Dolomite	0.13
LOI	2.58	Quartz	0.21

113

114   *2.2 Electric field application*

115

116   The electric field was applied by electrolytic cells similar to those for the chloride ion penetration tests described in

117   ASTM C1202 (Fig. 1a). The anode was a titanium mesh, and the cathode was a copper mesh. A constant electric

118   current of 30.0 mA (equal to ~4.71 A/m^2) was maintained by a DC power supply. The cells on both sides were

119   filled with the same sulfate solution, either 0.5 mol/L MgSO$_4$ or 0.5 mol/L Na$_2$SO$_4$. This concentration is slightly

120   higher than the one used in the sulfate expansion tests in ASTM C1012 (5% Na$_2$SO$_4$, ~0.35 mol/L). The solutions

121   were prepared using deionized water and sodium sulfate anhydrous (Sinopharm, purity > 99.0%) or magnesium

122   sulfate heptahydrate (Sinopharm, purity > 99.0%), and were refreshed every three days. An estimation based on

123   charge conservation shows that the concentration of the sulfate solutions can remain higher than ~0.34 mol/L

124   during the experiment (see Supplementary Data). For either MgSO$_4$ or Na$_2$SO$_4$, three sets of electrolytic cells were

125   set up. The specimens were taken out after exposure to the applied electric fields for 7, 14, and 28 days. The

126   deposits formed on the electrodes were cleaned every six days.

127
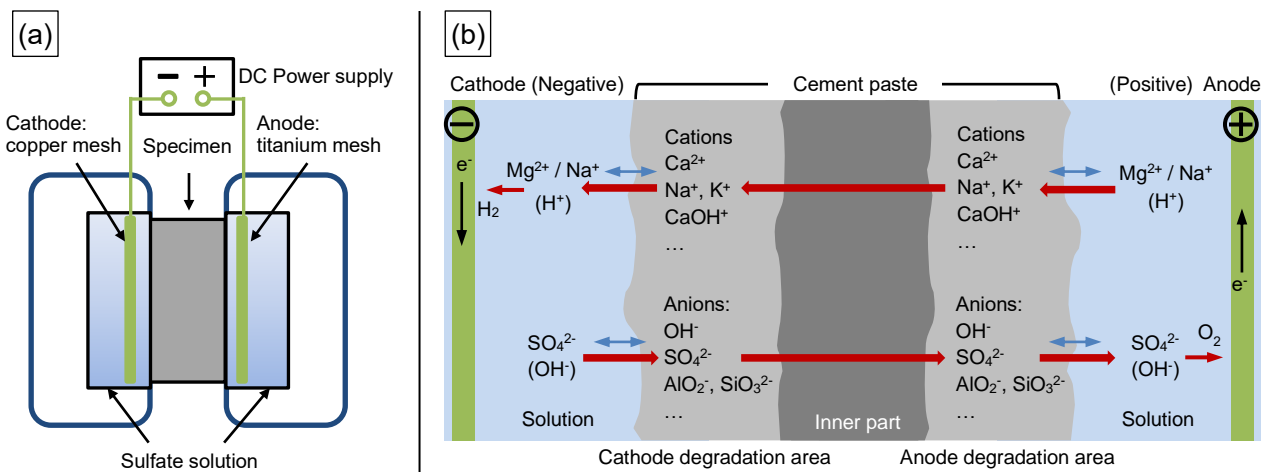
129 **Fig. 1.** Test setup to apply electric fields: (a) overview of the test setup and (b) schematic of ionic motion where
130 thickness and velocity are not to scale. The ionic motion is driven by electric migration (red arrows) and diffusion
131 (blue arrows).

132

133   Figure 1b illustrates the motion of ionic species in the test setup. The anode is connected to the positive output of

134   the power supply and has a higher electric potential compared with the cathode. The cations in the anodic solution

135   (Mg^{2+} or Na$^+$) migrate towards the cement paste and enter the specimen from the surface near the anode.

136   Meanwhile, the cations in the pore solution (Ca^{2+}, Na$^+$, K$^+$, etc.) migrate towards the cathode and leave the

137 specimen from the nearby surface. The anions migrate in the opposite direction. Diffusion also occurs in addition to

138 electric migration. The ionic species in the external solution (SO_4^{2-} and Na^+/Mg^{2+}) diffuse towards the specimen on

139 both sides, and the ions in the pore solution also diffuse towards the external solutions.

140

141 Similar test setups are also used in [39-41] for accelerating sulfate attacks in the laboratory. The current density was

142 not reported in those literatures, and the estimated values were between one and several A/m^2 based on the voltage

143 and size of the specimen (assuming the resistivity of water-saturated cement mortar is around 10 $k\Omega \cdot cm$). For

144 studying the effects of DC stray current on reinforcement corrosion and concrete degradation, the current densities

145 of 1 and 10 A/m^2 were chosen in [27,42]. The current density used in this paper (~4.71 A/m^2) is comparable to

146 these reported values.

147

148 *2.3 Test method*

149

150 After the exposures to the applied electric fields for certain durations, the specimens were removed from the test

151 setups and cut into pieces according to the procedures in Fig. 2. Small patches that contain all the depth from the

152 exposure surface (0 mm) to ~25 mm were prepared for SEM. A face perpendicular to the exposure surface was

153 used for observation. These samples were impregnated with epoxy resin, polished on SiC discs and diamond

154 suspension-sprayed discs (Buehler), carbon-coated, and observed using a Quanta 200 FEG microscope in the

155 backscattered electron mode. The hydration products on the surface of the specimens usually showed clear features

156 (brightness and morphology), and the chemical composition of such well-resolved hydration products was analyzed

157 based on at least five EDS measurements. EDS point analyses were also conducted randomly in the well hydrated

158 areas (where the hydration products mingle and cannot be identified easily) to reflect the chemical composition of

the hydration products in such areas. The average chemical composition in several 50 μm × 50 μm areas was

measured to represent the distribution of elements along the depth from the exposure surface. The microstructure

were analyzed by observing a 5-mm-wide area parallel to the surface.
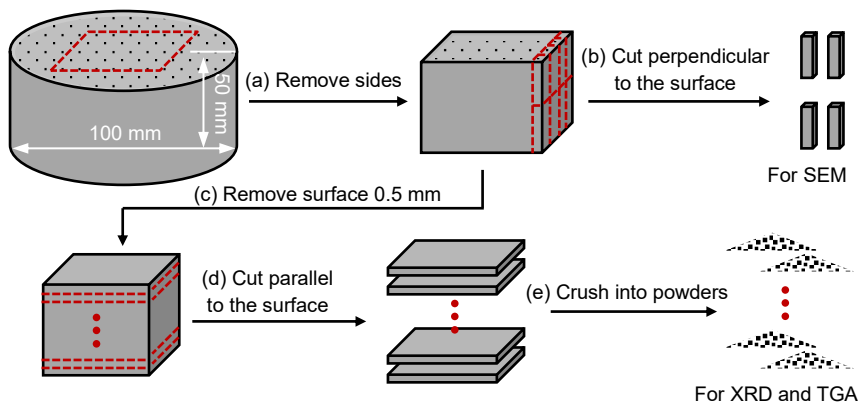
Fig. 2. Preparation of samples: (a) the sides of a cylindrical specimen that were not well exposed to sulfate
solutions were cut off, (b) small patches that were perpendicular to the exposure surface was cut for SEM, (c) the
surface part (0.5 mm) of the remainder was removed, (d) the specimen was cut parallel to the exposure surface into
5-mm thick slices, and (e) the slices were crushed into powders (particle size <75 μm) for XRD and TGA.

The powder samples for XRD and TGA were soaked in ethanol for 5 days to stop the hydration and then dried at

40 °C for 24 h. XRD was conducted on a D/max2550VB3+/PC diffractometer equipped with Cu $K_{\alpha 1}$ radiation and

a graphite monochromator. The X-ray generator was operated at 40 kV and 250 mA, the scanning range was $2\theta =$

5–75°, and the step size and counting time were 0.02° and 2 s, respectively. TGA was conducted on a NETZSCH

STA 449C simultaneous thermal analyzer. The samples were heated under N_2 atmosphere from 40 °C to 950 °C

with a heating rate of 10 °C/min. The data were expressed as differential thermogravimetry, and the peaks were

assigned according to [43]. Note that the specimens for XRD and TGA did not include the surface part (~0.5 mm),

because this part was quite different in composition from the other parts according to SEM but its material amount

was not sufficient for these tests.

179   *2.4 Rietveld refinement*

180

181   Corundum (α-Al$_2$O$_3$, Aladdin, purity > 99.99%) was used as an internal standard. It was mixed with the dried

182   powder samples at a mass ratio of 10 to 90. The Rietveld refinement was conducted using TOPAS Academic V5.

183   The crystallographic models were obtained from the Inorganic Crystal Structure Database (ICSD), see

184   Supplementary Data. The optimized parameters included the background coefficient, zero-shift error, crystal size L,

185   and lattice parameters (restrained within ± 0.5%). The peak shape was described by the fundamental parameter (FP)

186   approach employed in TOPAS. The March-Dollase ellipsoidal preferred orientation correction algorithm [44] was

187   employed for Alite-M3 (60$\underline{6}$) [45], portlandite (001) [46], and calcite (104) [45]. Two peaks using fundamental

188   parameters were added near 2θ = 29.3° and 50.0° to simulate the broad peaks produced by C-S-H [47,48]; and the

189   scale factor, crystal size L, and position of the peaks were refined.

190

191   *2.5 Simplifications in the thermodynamic modeling of the degradation process*

192

193   In order to gain insight into the chemical and mineralogical aspects of the degradation process and study the

194   degradation mechanism, a simplified approach was proposed to represent the main processes of electric migration.

195   Based on this simplified approach, the phase assemblage during degradation was further studied by thermodynamic

196   modeling. Here, electric migration is assumed to be the only driving force for the ionic motion and described by the

197   Nernst-Planck equation [22-25] as

$$J_{i,e} = -D_i^a \cdot \frac{z_i F}{RT} C_i \frac{\partial \Psi}{\partial x} \tag{1}$$

198   where $J_{i,e}$ (mol·m^{-2}·s^{-1}) is the bulk flux of ionic species i at location x; D_i^a (m^2·s^{-1}) is the apparent diffusion

199   coefficient; z_i is the charge number; C_i (mol·m^{-3}) is the ionic strength; $F = 9.648 \times 10^{-4}$ C·mol^{-1} is the Faraday

200　constant; $R = 8.314$ J·mol^{-1}·K^{-1} is the gas constant; T (K) is the absolute temperature; and Ψ (V) is the electric

201　potential. The apparent diffusion coefficient usually has a positive relationship with the corresponding diffusion

202　coefficient in free water (D_i^0 in m^2·s^{-1}), and this relationship is impacted by the pore structure characterized by

203　porosity (φ) and tortuosity (τ) as [23]

$$D_i^a = \frac{\varphi}{\tau^2} D_i^0 \tag{2}$$

204

205　When an electric field is applied, the migration rate of an ion depends on its charge number, concentration, and

206　diffusion coefficient in free water. The diffusion coefficient in free water can be obtained from the chemistry

207　handbook [49], and the concentration of ions in the cement paste before exposure to electric fields can be calculated

208　by thermodynamic modeling (see Supplementary Data), as shown in Table 2.

209

210　**Table 2** Concentration of ions in the pore solution before degradation and diffusion coefficient in free water (D_i^0).

	Concentration mol/L	Diffusion coefficient 10^{-9} m^2/s	Direction
OH$^-$	2.05×10^{-1}	5.273	
SO$_4^{2-}$	6.79×10^{-4}	1.065	
AlO$_2^-$	4.25×10^{-5}	n.a.[1]	
SiO$_3^{2-}$	9.94×10^{-6}	n.a.[1]	Cathode → inner part → anode → anodic solution
CO$_3^{2-}$	4.66×10^{-5}	n.a.[1]	
HCO$_3^-$	2.27×10^{-8}	1.185	
Ca^{2+}	1.01×10^{-3}	0.792	
Ca(OH)$^+$	9.09×10^{-4}	n.a.[1]	
Mg^{2+}	1.11×10^{-10}	0.706	Anode → inner part → cathode → cathodic solution
Na$^+$	2.34×10^{-3}	1.334	
K$^+$	2.01×10^{-1}	1.957	

211　[1] Not available in [49].

212

213　As illustrated in Fig. 1b, it is assumed that each specimen contains two degradation areas that are located on the

214　exposure surfaces and are affected by the chemical attack, while the inner part between these two degradation areas

215　is not affected. At the beginning of degradation, the pore solution chemistry and pore structure are similar in all

216   parts across the cement paste, and the electric gradient is uniform. In the pore solution, ionic species i at different

217   positions will migrate at the same rate according to Eq. 1. In the degradation area near the cathode, the cations are

218   released into the cathodic solution due to electric migration, but they are also supplemented by those migrating

219   from the inner part of the specimen at the same rate. The anions in the pore solution migrate towards the inner part

220   and are replaced by those from the cathodic solution. However, the migration rate of the anions from the cathodic

221   solution into the cement paste is difficult to determine, because the electric gradient and pore structure are different

222   between the surface of a specimen and its interior. Here, it is assumed that the replacement of the anions in the

223   degradation area near the cathode maintains the charge balance. Similarly, the main process in the degradation area

224   near the anode is the replacement of cations in the pore solution by those from the anodic solution in a

225   charge-balanced manner. These processes are similar to those reported in numerical simulation studies of the rapid

226   chloride migration test [23,50]. Here, they are defined as the "basic state" of electric migration, which is a transient

227   state when the concentration of the ions in the pore solution is similar to that before degradation initiates. The

228   duration of the basic state depends on whether the concentration of the ionic species in the pore solution remains

229   stable during the ionic exchange and the relevant chemical reactions.

230

231   In the pore solution, the concentration of OH^- is higher than the other anions by three orders of magnitude (Table 2),

232   and the main anion in the cathodic solution (a neutral Na_2SO_4 or $MgSO_4$ solution) is SO_4^{2-}. According to Eq. 1,

233   these two ionic species migrate much faster than the others in the pore solution and the cathodic solution,

234   respectively. Moreover, the decomposition of portlandite can somewhat help maintain the ionic strength of OH^- in

235   the pore solution, which is known as the buffering effect [51]. Therefore, the electric migration process near the

236   cathode is simplified to the replacement of each two moles of OH^- by one mole of SO_4^{2-}.

237

238   In the area near the anode, K^+ and Na^+ are the most easily migrated ionic species. However, they will be removed

239   quickly due to their low contents in the hydrated cement paste [23,50], indicating that this state is short-lived.

240   Afterward, Ca^{2+} will be the main ionic species to migrate. ($CaOH^+$ will also migrate, but its effect on the

241   mineralogical alteration is similar to that of Ca^{2+}.) Its ionic strength can be maintained by the buffering effect,

242   suggesting a possibly longer duration. Therefore, the electric migration process in this state is simplified by

243   replacing each mole of Ca^{2+} with one mole of Mg^{2+} or two moles of Na^+, based on a hydrated system without K

244   and Na.

245

246   *2.6 Thermodynamic modeling*

247

248   Thermodynamic modeling was performed using the geochemical code GEMS 3.3 [52] with the Nagra/PSI database

249   [53] and CEMDATA 18 database (version 18.01) [54]. The CSHQ model was selected. The solid solutions of AFt

250   and AFm were not considered. Siliceous hydrogarnet ($C_3AS_{0.8}H_{4.4}$) and thaumasite usually form at slow kinetics at

251   the ambient temperature [55,56]. The presence of electric fields does not significantly impact the slow formation

252   kinetics of thaumasite [57], but it remains unknown whether the formation kinetics of $C_3AS_{0.8}H_{4.4}$ will be

253   influenced. These products were both suppressed in the modeling.

254

255   First, the phase assemblage before sulfate ingress was calculated. The following hydration degrees were assumed

256   based on the XRD results at an age of 28 d: 95% for C_3S, 65% for C_2S, 100% for C_3A, and 70% for C_4AF. The

257   Na_2O and K_2O in the cement were assumed to dissolve completely, while the MgO was assumed to dissolve by

258   90%. Calcite was set to react freely [58].

259

260   The hydration phase assemblage during the electric migration process was then calculated by changing the input

261   recipe according to the simplified approach (see Supplementary Data). In order to further analyze the migration rate

262   of the ionic species in the pore solution during degradation, the theoretical flux of OH⁻ in the pore solution at the

263   beginning of degradation was considered as a reference. Provided that the pore structure in Eq. 2 does not change

264   significantly during degradation, the relative flux (R) of a type of ionic species i is hereby defined as

$$R = \frac{J_{i,e}}{J_{OH,e}} = \frac{D_i^0 z_i C_i}{D_{OH}^0 z_{OH} C_{OH}^o} \tag{3}$$

265

266   At a given time during the electric migration process, an ion with higher relative flux migrates faster, provided that

267   the flux is uniform in the cross-section. In addition to their migration, the concentration of ions in the pore solution

268   may also be affected by the phase changes induced by electric migration, and the manner of ionic migration may

269   thus deviate from the description of the simplified processes. This effect can also be represented by the changes in

270   the relative flux.

271

272   **3 Results**

273   *3.1 Test results of MgSO₄ exposure*

274   3.1.1 Chemical composition and microstructural alterations

275

276   Near the cathode, an exposure to MgSO₄ in the presence of applied electric fields increased the S content of the

277   cement paste (Fig. 3, see from the left). The S content near the surface (e.g., 0.1–10 mm) increased with the

278   exposure time and became higher than that of the inside part (e.g., 20 mm). In addition, the Ca content near the

279   surface decreased whilst the Si and Al contents increased. An enrichment of Mg was observed at a depth of 0.1–

280   0.25 mm after an exposure time of 28 d (Fig. 3b). In addition to the chemical composition alteration, the surface

area near the cathode (0–3 mm) showed a layered microstructure (Fig. 4a). In the outermost layer (0–300 μm, area

I), a large amount of $CaSO_4$ formed on the surface of the specimen, and the hydration products decalcified to form

silica-alumina gel (e.g., Spot A of Fig. 4b). Deeper inside the cement paste (300–1000 μm, area II), the hydration

products were affected by both decalcification and magnesium ingress. The silica-alumina gel showed a high Mg

content (Spot A of Fig. 4c), which agrees with the Mg enrichment in this area (Fig. 3b). $CaSO_4$ was also present in

this area (Spot B of Fig. 4c). About 1–3 mm from the surface (area III), the hydration products were not impacted

by the ingress of either magnesium or sulfate. The cement paste was porous (Fig. 4d). The Ca/Si ratio of the

hydration products in this area was typically smaller than 1.5, which coincides with the chemical composition

shown in Fig. 3b. From 3 mm inside (area IV), the cement paste started to show continuous alterations without
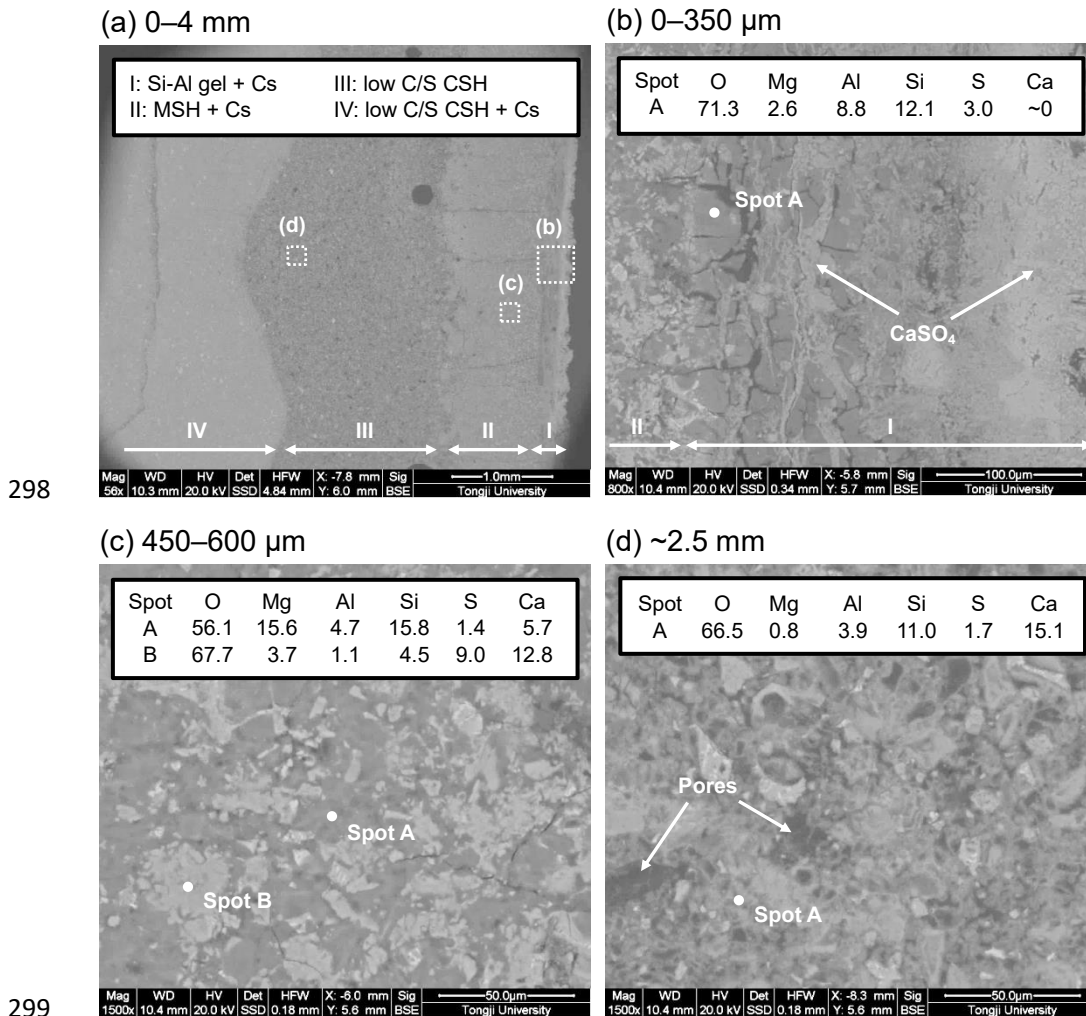
layered structures.
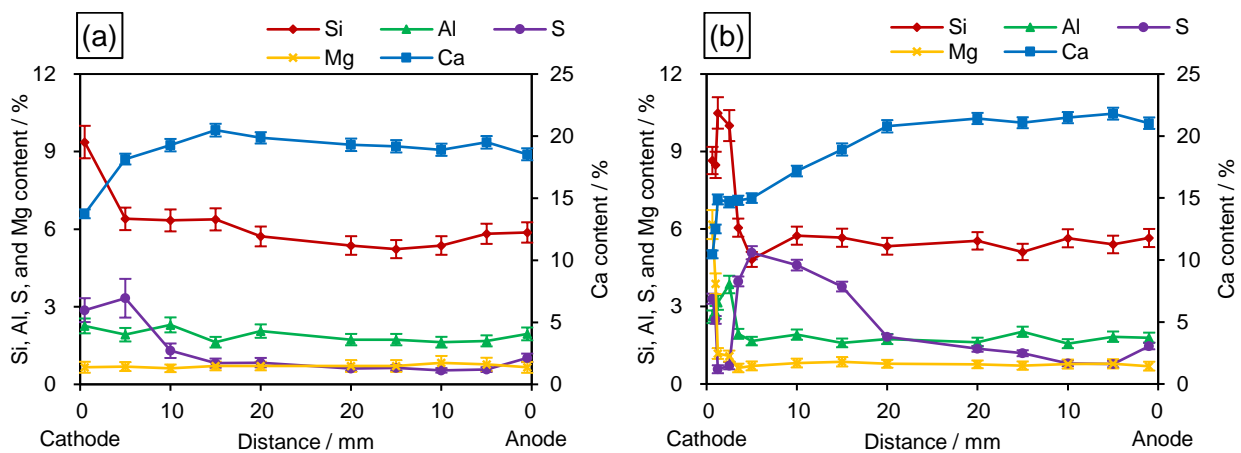
Fig. 3. Chemical composition at different distances from the surface (cathode on the left and anode on the right) after exposure to $MgSO_4$ for (a) 7 d and (b) 28 d. Each data point represents the average over a 50 μm × 50 μm area measured by EDS. Error bars indicate the standard error in ZAF matrix correction schemes. The sampling points nearest to the surfaces are 0.1 mm from the surface.

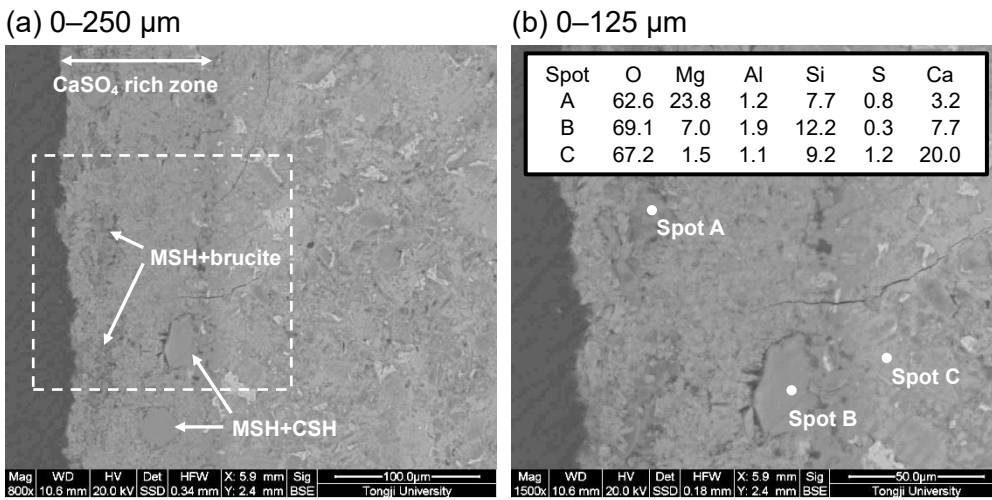**(a) 0–4 mm**

I: Si-Al gel + Cs	III: low C/S CSH
II: MSH + Cs	IV: low C/S CSH + Cs

(d)

(b)

(c)

IV   III   II   I

Mag	WD	HV	Det	HFW	X: -7.8 mm	Sig	——1.0mm——
56x	10.3 mm	20.0 kV	SSD	4.84 mm	Y: 6.0 mm	BSE	Tongji University

(b) 0–350 µm

Spot	O	Mg	Al	Si	S	Ca
A	71.3	2.6	8.8	12.1	3.0	~0

Spot A

CaSO$_4$

II   I

Mag	WD	HV	Det	HFW	X: -5.8 mm	Sig	——100.0µm——
800x	10.4 mm	20.0 kV	SSD	0.34 mm	Y: 5.7 mm	BSE	Tongji University

(c) 450–600 µm

Spot	O	Mg	Al	Si	S	Ca
A	56.1	15.6	4.7	15.8	1.4	5.7
B	67.7	3.7	1.1	4.5	9.0	12.8

Spot A

Spot B

Mag	WD	HV	Det	HFW	X: -6.0 mm	Sig	——50.0µm——
1500x	10.4 mm	20.0 kV	SSD	0.18 mm	Y: 5.6 mm	BSE	Tongji University

(d) ~2.5 mm

Spot	O	Mg	Al	Si	S	Ca
A	66.5	0.8	3.9	11.0	1.7	15.1

Pores

Spot A

Mag	WD	HV	Det	HFW	X: -8.3 mm	Sig	——50.0µm——
1500x	10.4 mm	20.0 kV	SSD	0.18 mm	Y: 5.6 mm	BSE	Tongji University

Fig. 4. Microstructure of the surface area (0–4 mm) near the cathode after 28 d exposure to MgSO$_4$: (a) an overview, and (b) to (d) enlargements of the squared areas. Surface on the right.

The cement paste near the anode did not show significant alterations on both chemical composition (Fig. 3, see from the right) and microstructure (Fig. 5). A very small increase of the S content was observed in the surface area (0.1 mm from the surface). Considering the direction of electric migration (Fig. 1b), the increased S content is mainly induced by diffusion [39,40]. The Mg^{2+} in the anodic solution should theoretically move towards the cement paste due to electric migration (Fig. 1b). However, the ingress of Mg^{2+} was constrained within a depth of ~100 µm according to SEM. (Fig. 5). This 100-µm-zone was rich in CaSO$_4$, and two types of Mg-containing products with different brightness and Mg/Si ratio were found. Closer to the surface, some Mg-containing products in clusters were embedded in the CaSO$_4$. These products were darker than the hydration products nearby. The Mg/Si ratio was

higher than 3 (Spot A), which potentially indicates a mixture of M-S-H and brucite on the microscale. Similar

products were also reported to form on the surface of the cement mortar after the magnesium sulfate attack in the

absence of applied electric fields [15,16]. Farther from the exposure surface, there were some larger particles (Spot

B). Compared with the Mg-containing products in clusters (Spot A), the Mg/Si ratio of these particles was much

lower, and the Ca content was higher. This chemical composition led to a slightly higher brightness and may

represent a mixture of M-S-H and C-S-H, or an M-C-S-H [59]. Next to the $CaSO_4$-rich zone, the Ca/Si ratio of the

hydration products was typically higher than 1.5, and no magnesium-containing products were observed, which is

also verified in Fig. 3b.

(a) 0–250 μm

(b) 0–125 μm

Spot	O	Mg	Al	Si	S	Ca
A	62.6	23.8	1.2	7.7	0.8	3.2
B	69.1	7.0	1.9	12.2	0.3	7.7
C	67.2	1.5	1.1	9.2	1.2	20.0

Fig. 5. Microstructure of the surface area (0–250 μm) near the anode after 28 d exposure to $MgSO_4$: (a) an overview and (b) enlargement of the squared area. Surface on the left.

EDS spot analyses were conducted randomly at certain depths, and the S/Ca is plotted against the Al/Ca in Fig. 6.

After an exposure time of 7 d (Fig. 6a), the chemical composition of the hydration products indicates the presence

of $CaSO_4$ and ettringite at the depths of 0.5 mm and 5 mm from the cathode. A small amount of ettringite may exist

at the depth of 15 mm. After an exposure time of 28 d (Fig. 6b), the hydration products at 2 mm from the cathode

(area III, Fig. 4a) showed very small S/Ca and relatively high Al/Ca to the other groups, coinciding with the

329   decalcification observed in Spot A, Fig. 4d. $CaSO_4$ was suggested to be the dominant sulfate-bearing phase at 5 mm

330   from the cathode (area IV, Fig. 4a), and a large amount of $CaSO_4$ with ettringite in a minor proportion may be

331   paresnt at 15 mm from the cathode. In the areas that are 0.5 mm, 5 mm, and 15 mm from the anode (Fig. 6c), the

332   hydration products may contain a mixture of ettringite, monosulfate, C-S-H, and portlandite.

333

334
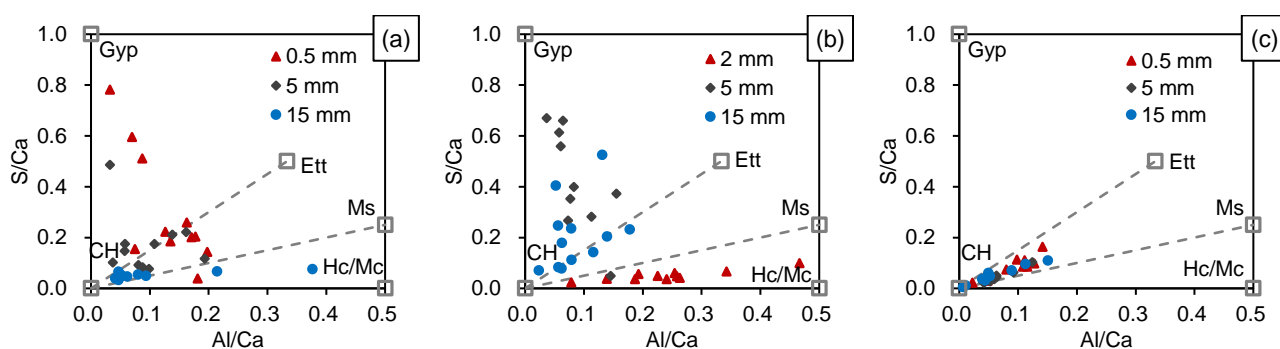
Fig. 6. Atom ratio plots of S/Ca against Al/Ca at different depths from the surface after exposures to $MgSO_4$: (a)
and (b) the cathode areas exposed to $MgSO_4$ for 7 d and 28 d, respectively; (c) the anode areas exposed to $MgSO_4$
for 28 d. CH = Portlandite (and C-S-H at a similar position), Ett = Ettringite, Ms = Monosulfate, Hc/Mc =
Hemicarbonate or monocarbonate, Gyp = $CaSO_4$.

339

340   3.1.2 Mineralogical alteration

341

342   In the cement paste near the cathode, the formation of sulfate-bearing products and decomposition of portlandite

343   were observed. After 28 d exposure to $MgSO_4$, the cement paste nearest to the surface (0.5–5 mm) contained almost

344   no portlandite or ettringite, but a large amount of $CaSO_4$ (Fig. 7a, see from the left). The $CaSO_4$ content was

345   slightly higher at 5–10 mm than that of the surface part, and started to decrease beyond this depth. Portlandite and

346   ettringite were detected beyond the depth of 10 mm, and their contents increased with the depth. In addition to the

347   decomposition of portlandite, the amorphous content in the cement paste near the cathode also showed a reduction.

348   Fig. 7b shows that the formation of ettringite and $CaSO_4$ started even before 7 d, during which the decomposition

349   of portlandite had been significant. Between 7–14 d, the formation of $CaSO_4$ continued while ettringite started to

350   decompose. Almost no portlandite could be detected by 14 d, and the $CaSO_4$ content remained almost constant

351   afterward. Monocarbonate and hemicarbonate were observed due to the hydration of limestone [56,58]. These

352   products had formed before the exposure to $MgSO_4$ but started to decompose after the exposure. Almost no AFm

353   phases remained near the cathode after an exposure time of 7 d (Fig. 7b). Magnesium-bearing products were not

354   observed in XRD, which agrees with the small penetration depth of Mg^{2+} shown in Fig. 3 and Fig. 4. However,

355   brucite was observed to form in the cathodic solution, which mingles with other products and forms a thick layer of

356   deposits on the electrode. The deposits collected on the 28th exposure day and tested by XRD suggested a mixture

357   of 40.2% brucite, 41.1% gypsum, 14.5% portlandite, 3.3% anhydrite, and 0.8% calcite.

358
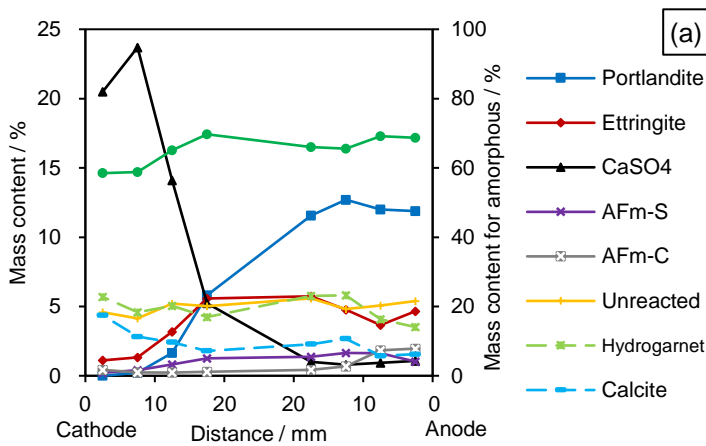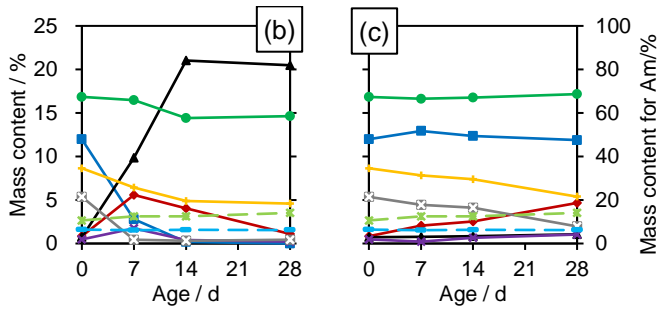
361   **Fig. 7.** Mineralogical composition of the specimen exposed to $MgSO_4$ obtained by XRD and Rietveld refinement:
362   (a) all the depths after 28 d exposure time; (b) and (c) phase alteration of the 0.5–5 mm area near the cathode and
363   anode, respectively, after different exposure time. $CaSO_4$ = anhydrite + bassanite + gypsum, AFm-S = monosulfate,
364   AFm-C = monocarbonate + hemicarbonate, hydrogarnet = katoite + hydrogrossular.

365

366   In the anode area, the ettringite content in the 0.5–5 mm area increased slowly with the exposure time, and the

367 contents of monocarbonate and hemicarbonate decreased (Fig. 7c). After 28 d, the ettringite content in this area was

368 slightly higher than that of the 5–10 mm area (Fig. 7a, see from the right). No other significant mineralogical

369 alterations could be observed in the 0.5–5 mm area, which also agrees with the SEM observations (Fig. 3, Fig. 5,

370 and Fig. 6c). The XRD analyses did not include the outer surface (~0.5 mm) and thus no Mg-bearing product, e.g.,

371 brucite, was detected. No brucite deposits could be found in the anodic solution, either.

372

373 The XRD results are also confirmed by TGA, as detailed in Supplementary Data.

374

375 *3.2 Test results of Na_2SO_4 exposure*

376 3.2.1 Chemical composition and microstructural alterations

377

378 Near the cathode, an exposure to Na_2SO_4 in the presence of applied electric fields also induced an increased S

379 content (Fig. 8, see from the left), but to a much lower extent compared with the situation of the $MgSO_4$ exposure

380 (Fig. 3). The S content in the 0.5–10 mm area after 28 d exposure to Na_2SO_4 (Fig. 8b) was even lower than that of

381 the same area exposed to $MgSO_4$ for 7 d (Fig. 3a). Different from the situation of $MgSO_4$ exposure, the loss of Ca^{2+}

382 in this area could not be clearly observed. After an exposure time of 28 d, the Ca content on the surface even

383 showed a small increase (Fig. 8b). The microstructure of the cement paste after the exposure to Na_2SO_4 showed

384 different features compared with that of the $MgSO_4$ exposure. The cement paste in the 0–600 μm area was porous

385 (Fig. 9a). Portlandite and large ettringite crystals could be observed (Fig. 9b). A calcite shell covered the surface of

386 the specimen, and calcite could also be found inside the cement paste.

387
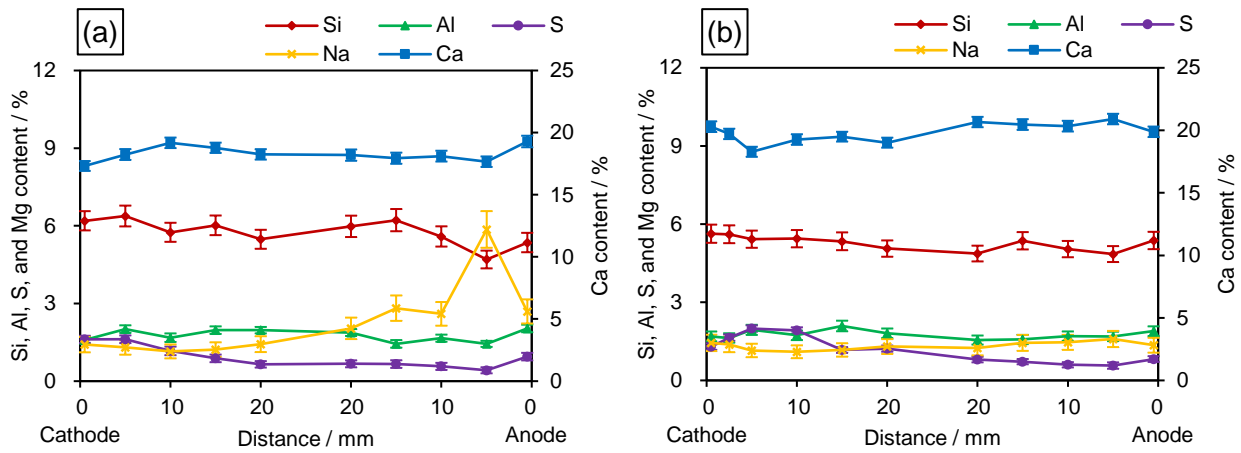
Fig. 8. Chemical composition at different distances from the surface (cathode on the left and anode on the right) after exposure to Na_2SO_4 for (a) 7 d and (b) 28 d.

The surface area near the anode (0.5 mm) showed slightly higher S content compared with the areas inside the specimen (Fig. 8, see from the right), which is similar to the situation of $MgSO_4$ exposure. Different from Mg^{2+} whose penetration depth is less than 100 μm, Na^+ could penetrate deeper into the specimen from the anode, as indicated by its increased content at a depth of 5–15 mm near the anode in Fig. 8a. There are two possible causes for the Na enrichment: a) a continuous accumulation during seven days, or b) a quick accumulation during the day before testing, after the sulfate solution was just refreshed. When we chose not to refresh the solution on the 27th day, no Na enrichment was observed in the specimen on the 28th day (Fig. 8b). This observation supports the second hypothesis and indicates that the migration of Na^+ under electric fields was fast. The microstructure of the surface area after Na_2SO_4 exposure showed some similar features compared with that of $MgSO_4$ exposure. A $CaSO_4$-rich zone also formed (Fig. 10a), and silica gel that is rich in Na can be observed (Spot A of Fig. 10b). Between the $CaSO_4$-rich zone and the cement paste, there is a Na-bearing rim (Spot B of Fig. 10b). Comparing th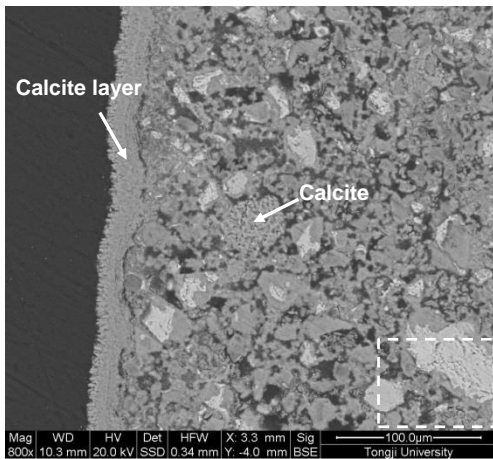e chemical composition of the rim with that of the Na-rich silica gel, the former owned a slightly lower Na content and a higher Ca content. Next to the $CaSO_4$-rich zon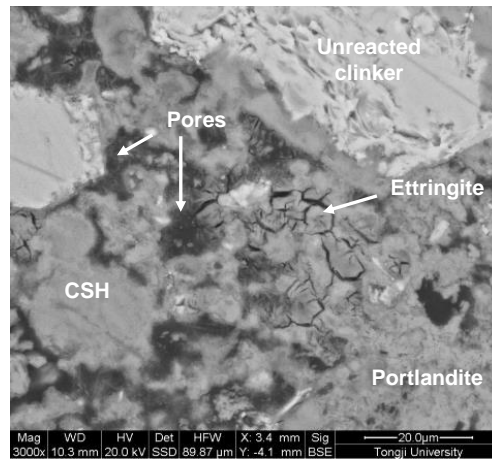e, the Ca/Si ratio of the hydration products was also higher than 1.5. The Ca/Si ratio became stable beyond this depth (~100 μm), as also verified in Fig. 8b.

(a) 0–250 μm

(b) ~250 μm

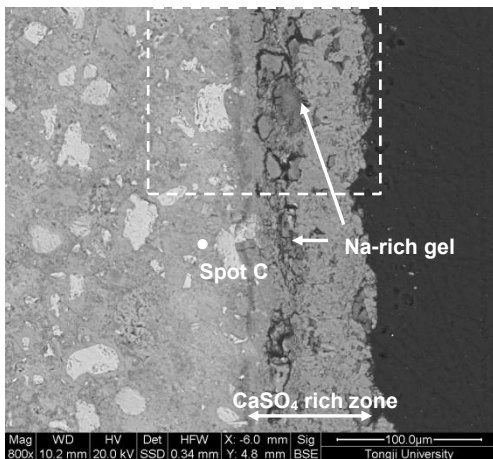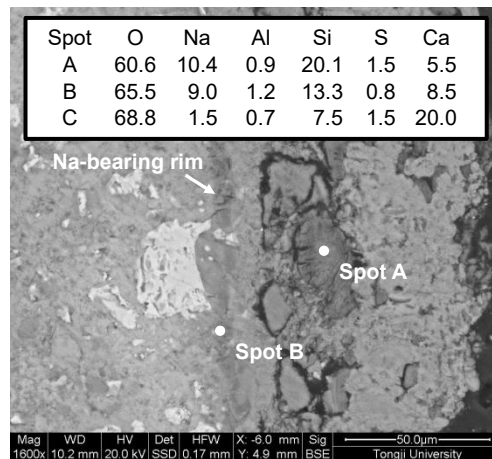**Fig. 9.** Microstructure of the surface area (0–250 μm) near the cathode after 28 d exposure to Na_2SO_4: (a) an overview and (b) enlargement of the squared area. Surface on the left.

(a) 0–250 μm

(b) 0–125 μm

Spot	O	Na	Al	Si	S	Ca
A	60.6	10.4	0.9	20.1	1.5	5.5
B	65.5	9.0	1.2	13.3	0.8	8.5
C	68.8	1.5	0.7	7.5	1.5	20.0

Fig. 10. Microstructure of the surface area (0–250 μm) near the anode after 28 d exposure to Na_2SO_4: (a) an overview and (b) enlargement of the squared area. Surface on the right.

The S/Ca plotted against Al/Ca indicates the presence of ettringite in large amounts at 0.5 mm and 5 mm depths from the cathode when the specimen is exposed to Na_2SO_4 for 7 d (Fig. 11a). After an exposure time of 28 d, ettringite was suggested to form at 0.5 mm, 5 mm, and 15 mm depths from the cathode (Fig. 11b), whilst a small amount of ettringite may also be present at the 0.5 mm area from the anode (Fig. 11c).
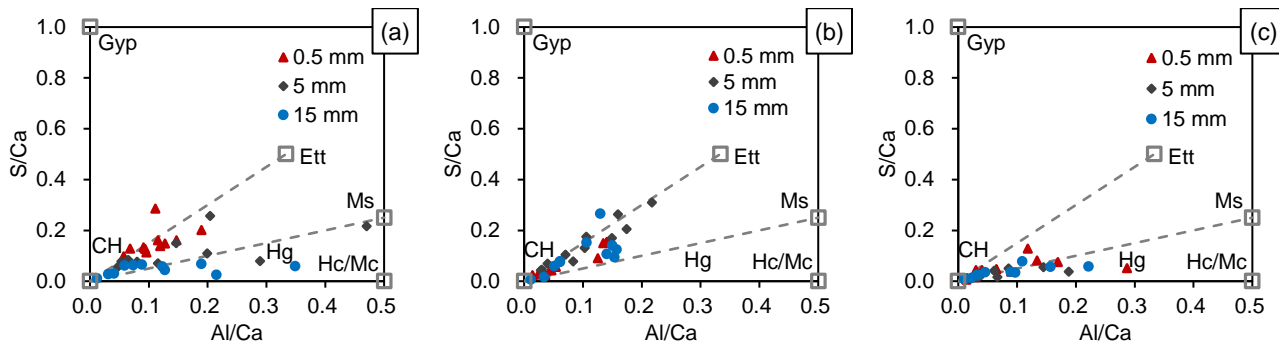
Fig. 11. Atom ratio plots of S/Ca against Al/Ca at different depths from the surface after exposures to Na_2SO_4: (a) and (b) the cathode areas exposed to Na_2SO_4 for 7 d and 28 d, respectively; (c) the anode areas exposed to Na_2SO_4 for 28 d. CH = Portlandite (and C-S-H at a similar position), Ett = Ettringite, Ms = Monosulfate, Hc/Mc = Hemicarbonate or monocarbonate, Gyp = $CaSO_4$.

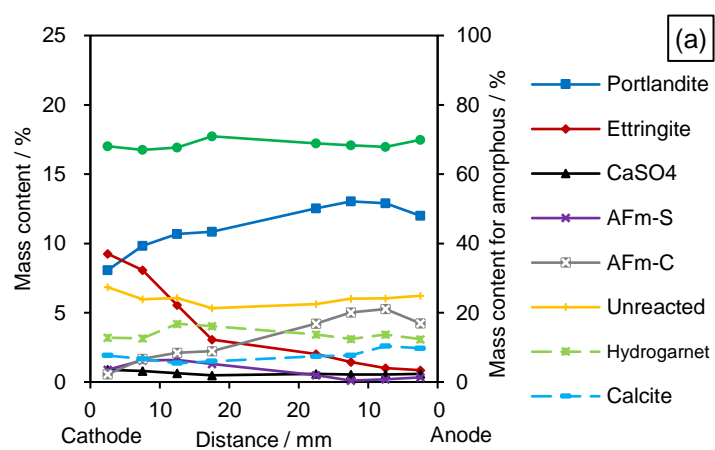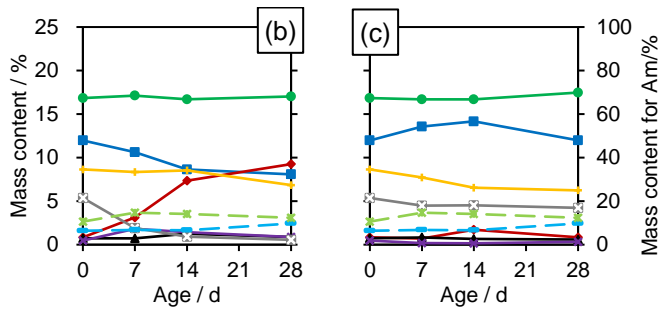3.2.2 Mineralogical alteration

When the specimen is exposed to Na_2SO_4, $CaSO_4$ did not form in large amounts near the cathode (e.g., 0.5–20 mm, Fig. 12a, see from the left) even after an exposure time of 28 d. Instead, the ettringite content in this area was high, and it decreased with the distance from the surface. Furthermore, the decomposition of portlandite and AFm (especially monocarbonate and hemicarbonate) after Na_2SO_4 exposure was not as significant as the situations in the $MgSO_4$ exposure (comparing Fig. 12a to Fig. 7a). The decomposition of portlandite and AFm, and the formation of ettringite showed a positive relationship with time (Fig. 12b).

Fig. 12. Mineralogical composition of the specimen exposed to Na_2SO_4 obtained by XRD and Rietveld refinement: (a) all the depths after 28 d exposure time; (b) and (c) phase alteration of the 0.5–5 mm area near the cathode and anode, respectively, after different exposure time. $CaSO_4$ = anhydrite + bassanite + gypsum, AFm-S = monosulfate, AFm-C = monocarbonate + hemicarbonate, hydrogarnet = katoite + hydrogrossular.

In the surface area near the anode (0.5–5 mm), no significant mineralogical alterations could be observed except for a small increase in the ettringite content and a decrease in the contents of monocarbonate and hemicarbonate. Similar to the situation of $MgSO_4$ exposure, these phenomena are assigned to the effects of SO_4^{2-} diffusing from the anodic solution (Fig. 12c). The Na enrichment after 7 d exposure to Na_2SO_4 did not form any products that can be detected by XRD. Moreover, no deposits formed in the cathodic and anodic solutions.

3.3 Results of thermodynamic modeling

3.3.1 Phase assemblage and pore solution chemistry

The phase assemblage and pore solution chemistry during the simplified electric migration processes were calculated by thermodynamic modeling. For the electric migration near the cathode (Fig. 13a), SO_4^{2-} initially stabilized ettringite in favor of monocarbonate. After the complete consumption of monocarbonate, gypsum was stabilized in favor of portlandite and C-S-H. During these processes, the SO_4^{2-} concentration in the pore solution showed an increase, whilst the OH^- concentration kept decreasing (Fig. 13b). In addition to gypsum, amorphous

457   SiO$_2$ and AH$_3$ were predicted as the stable phases at the last stage of the electric migration process.

458

459

460

461

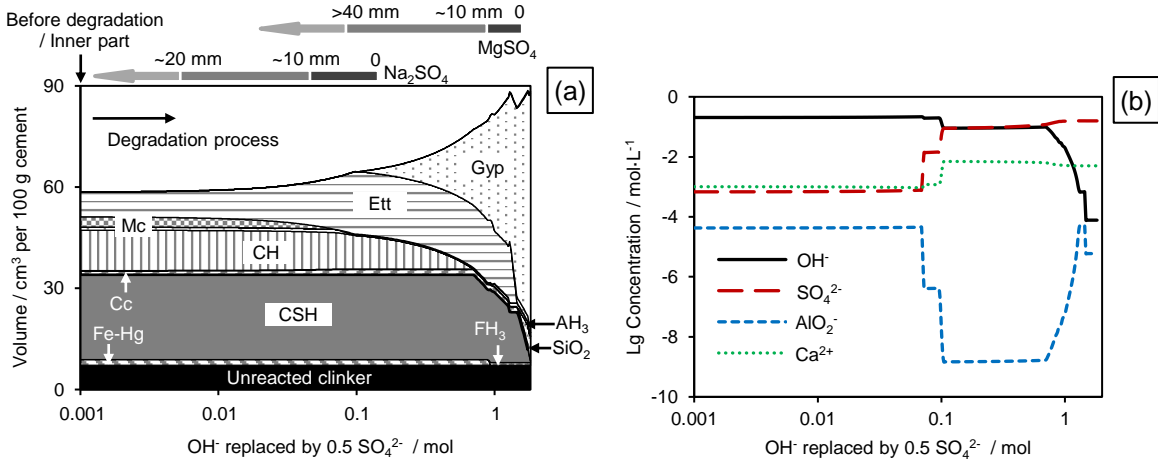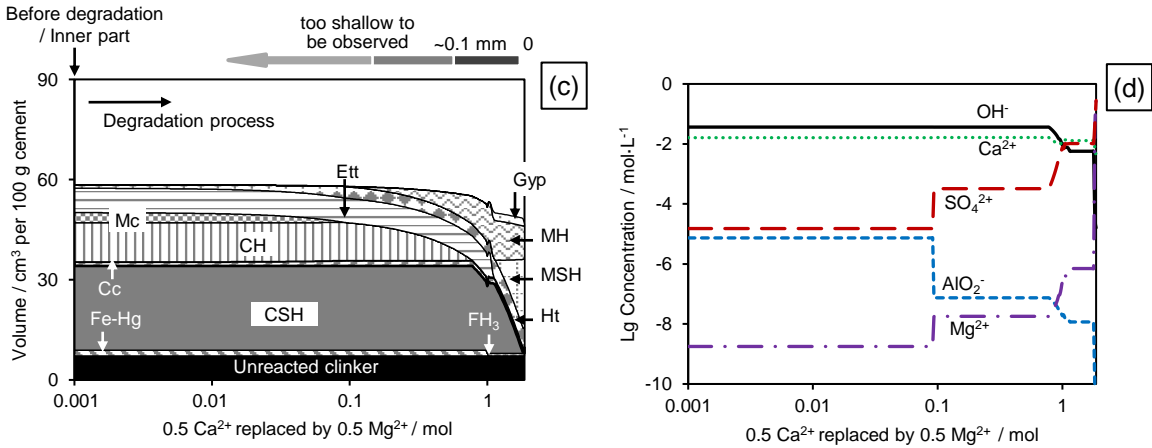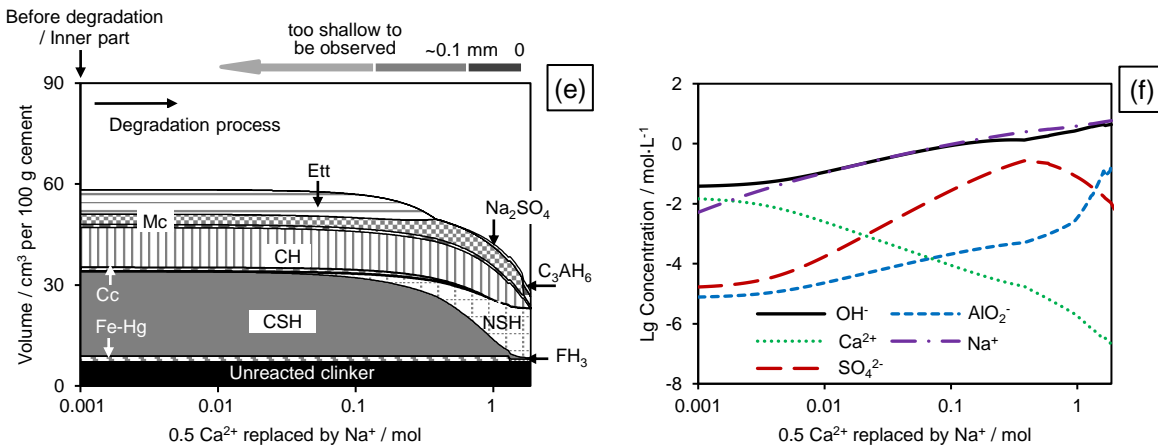**Fig. 13**. Phase assemblage and pore solution chemistry during the simplified electric migration process, calculated by thermodynamic modeling: (a) and (b) the degradation process near the cathode; (c) and (d) the degradation process near the anode after MgSO$_4$ exposure; (e) and (f) the degradation process near the anode after Na$_2$SO$_4$ exposure. The horizontal-axis can be interpreted into the alteration in a certain position with time or the distribution of products after a certain exposure time. A logarithmic axis is used for better comparison with thermodynamic modeling studies on diffusion-induced sulfate attacks [1,2,11,14-16]. The arrows above the figures illustrate the

approximate distribution of hydration products after 28 d exposure time (experimental results). CH = portlandite, Ett = ettringite, Mc = monocarbonate, Gyp = gypsum, Cc = calcite, Fe-Hg = $C_3FS_{0.84}H_{4.32}$ and/or $C_3F_{1.34}H_{3.32}$, Ht = hydrotalcite, MH = brucite, MSH = M-S-H gel, and NSH = the Na end-member, $[(NaOH)_{2.5}SiO_2H_2O]_{0.2}$ included in the CSHQ model.

In the anode area exposed to $MgSO_4$ (Fig. 13c), the incorporated Mg^{2+} stabilized hydrotalcite and ettringite in favor of monocarbonate at an initial stage. Brucite formed when all the monocarbonate was consumed, during which portlandite decomposed. At the last stage of the electric migration process, M-S-H and gypsum were stabilized in favor of C-S-H and ettringite, respectively. In contrast, exposure to Na_2SO_4 induced continuous Na uptake in the C-S-H (Fig. 13e). By separating the Na end-member from the C-S-H phase in the CSHQ model, the Na uptake can be clearly observed. Portlandite kept stable until the depletion of C-S-H. Ettringite and monocarbonate were predicted to destabilize during the electric migration process.

3.3.2 Migration of ionic species

The simplified electric migration process assumes that the phase changes are restricted in a certain "degradation area" on the surface of a specimen (see Fig. 1b). The relative flux of a certain ion is thus interpreted as its migration rate from the degradation area towards a certain direction which depends on the ion's polarity. In the degradation area near the cathode, when degradation initiated OH^- had the highest relative flux among all the ionic species (Fig. 14a). This phenomenon demonstrates that the replacement of OH^- by SO_4^{2-} from the external solution was the most significant process that occurred. The relative flux of SO_4^{2-} turned higher when all the monocarbonate decomposed (point A), and exceeded that of OH^- when portlandite started to decompose and gypsum started to form (point B). From this point on, SO_4^{2-} would take the place of OH^- as the main ionic species that migrated towards the inner part of the specimen. The replacement of OH^- by SO_4^{2-} in the degradation area, represented by the relative flux of OH^-,

492   thus slowed down, and the degradation remained stable at point B. During the degradation process, the relative flux

493   of Ca^{2+} showed an increase (point A), indicating that the loss of Ca^{2+} from the degradation area to the external

494   solution will be faster than the compensation from the inner part of the specimen.

495

496

497

498

499   **Fig. 14.** The relative flux of ionic species: (a) the cathode area; (b) and (c) the anode area exposed to $MgSO_4$ and
500   Na_2SO_4, respectively. The cations and anions migrate in different directions, see Fig. 1b. Certain ionic species are
501   compensated by those from the inner part of the specimen, and the compensation rate is marked by a diamond
502   (provided that the ionic strength in the inner part of the specimen remains stable). The square bracket indicates the
503   ionic species in the external solution is transported into the degradation area with the same relative flux to certain
504   ions based on the assumption of charge balance.

505

506   For the anode area that is exposed to $MgSO_4$ (Fig. 14b), the relative flux of OH^- remained the highest for a long

507   period during the electric migration process. This phenomenon indicates that the outflow of OH^- to the external
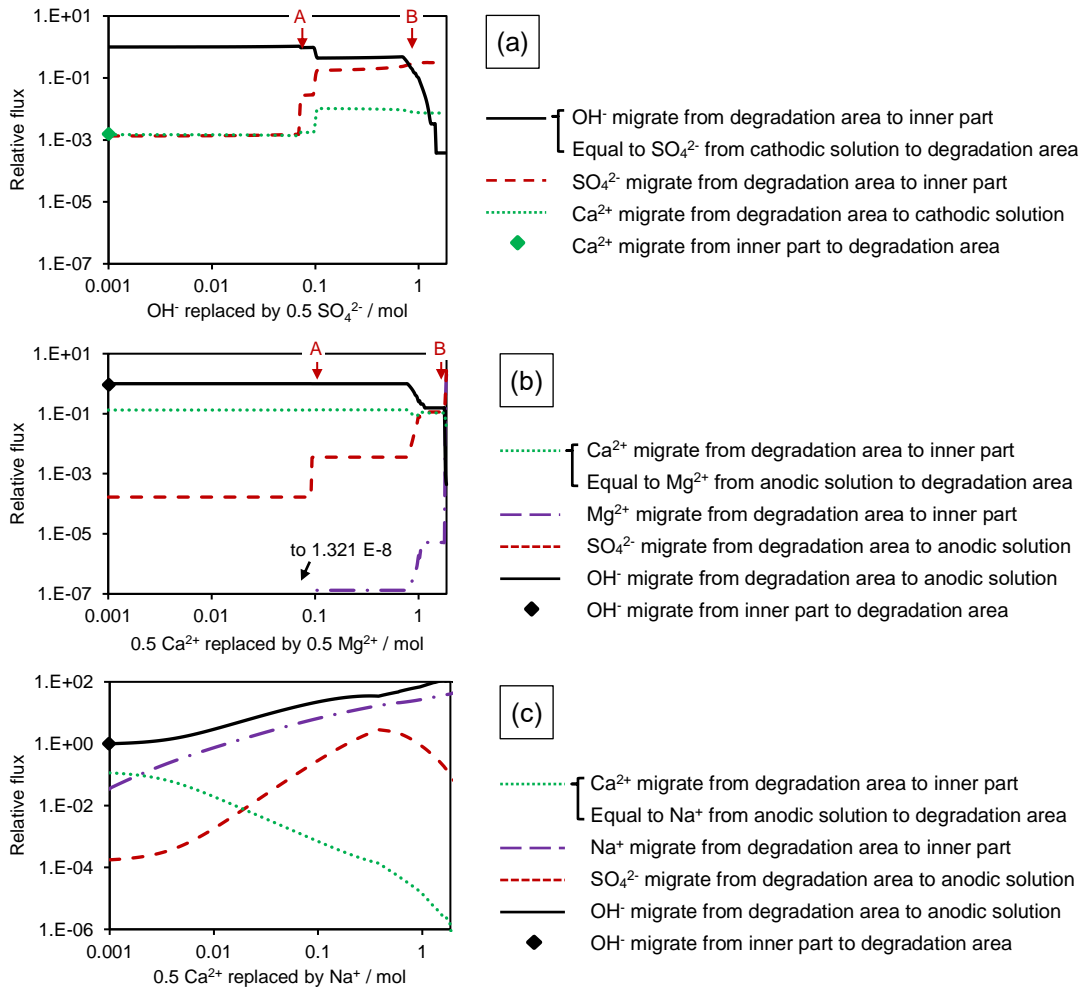
508   solution, as well as the compensation of OH⁻ from the inner part, was faster than the migration of all the other ions.

509   The relative flux of Ca^{2+} was at a lower level, indicating that the Ca^{2+} in the degradation area would be replaced by

510   the Mg^{2+} from the external solution at a slow rate. The relative flux of Mg^{2+} was even lower than that of Ca^{2+},

511   indicating that the Mg^{2+} in the degradation area could hardly migrate towards the inner part. The relative flux of

512   SO_4^{2-} showed an increase during the electric migration process (point A). This phenomenon will theoretically lead

513   to a loss of SO_4^{2-} in the degradation area, but this effect may be offset by the diffusion of SO_4^{2-} from the external

514   solution in the experiments. At the last degradation stage (point B), the relative flux of Mg^{2+} increased sharply, the

515   penetration of Mg^{2+} started, and the entire electric migration process repeated stepwise in a slightly deeper area

516   from the surface. The degradation phase assemblage thus kept stable at point B.

517

518   When the anode was exposed to Na_2SO_4 (Fig. 14c), the relative flux of OH⁻ remained the highest among all the

519   ionic species during the entire electric migration process. The relative flux of Na^+ was lower than that of OH⁻, but

520   much higher than that of Mg^{2+} in the specimen exposed to $MgSO_4$. This phenomenon indicates that Na^+ will

521   migrate into the cement paste at a much higher rate than Mg^{2+}. The relative flux of Ca^{2+} was at a low level during

522   the electric migration process, suggesting that the replacement of Ca^{2+} by Na^+ in the degradation area will be slow,

523   and most Na^+ will migrate towards the inner part of the specimen.

524

525   **4 Discussions**

526   *4.1 Comparison between test results and thermodynamic modeling*

527

528   The mineralogical alterations that occurred near the cathode agreed well with the thermodynamic modeling, as

529   indicated by the arrows in Fig. 13a. After exposure to $MgSO_4$ for 28 d, $CaSO_4$ was observed to form in the outer

530 part of the specimen (0–10 mm) where almost no portlandite or ettringite existed (XRD, Fig. 7a). The

531 silica-alumina gel found on the surface of the specimen (SEM, Fig. 4b) corresponds to the amorphous SiO_2 and

532 AH_3 in the thermodynamic modeling [14], and the reduction of the amorphous content coincides with the

533 decomposition of C-S-H predicted by thermodynamic modeling. Deeper inside the specimen (10–40 mm), the

534 content of $CaSO_4$ gradually decreased, while those of portlandite and ettringite increased (XRD, Fig. 7a). In

535 comparison, the specimen exposed to Na_2SO_4 for 28 d remained at an earlier degradation stage, when $CaSO_4$ did

536 not form in large amounts. The different degradation stages between the specimens also coincide with the amount

537 of S that has been transported from the cathodic solution into the cement paste (EDS, cf. Fig. 3b and Fig. 8b).

538

539 The mineralogical alterations occurred in a shallow depth (~0.1 mm) in the cement paste near the anode, but had

540 proceeded to the last degradation stage in both exposure conditions when comparing the test results with the

541 thermodynamic modeling (Fig. 13c and 13e). For the $MgSO_4$ exposure, the presence of Mg-containing products

542 (brucite and M-S-H, SEM, Fig. 5) agrees with the thermodynamic calculation, while for the Na_2SO_4 exposure, the

543 Na-rich silica gel (Fig. 10) coincides with the Na uptake by C-S-H in the thermodynamic modeling. A $CaSO_4$-rich

544 zone was observed in both exposure conditions no matter if $CaSO_4$ is predicted to be stable. The diffusion of SO_4^{2-}

545 from the anodic solution is believed to be responsible for this phenomenon (see also Fig. 1b).

546

547 *4.2 Migration behavior of Mg^{2+}, Na^+, and SO_4^{2-}*

548

549 The degradation near the cathode and anode proceeded in different ways. Near the cathode, the anions from the

550 external solution (mainly SO_4^{2-}) migrated into a deep area, and the mineralogical alteration proceeded gradually

551 following the prediction of thermodynamic modeling. For the anode area exposed to $MgSO_4$, the incorporation of

552   Mg^{2+} occurred in a shallow area with the mineralogical alteration proceeding directly to the late degradation stage.

553   In contrast, Na^+ could penetrate deep into the cement paste, but the mineralogical alteration occurred also in a

554   shallow area. The different migration behaviors of the ionic species can be explained by the relative flux which is

555   obtained from the solution chemistry calculated by thermodynamic modeling.

556

557   According to section 3.3.2, an ion's capability for migration under electric fields depends on its relative flux, while

558   its accumulation rate in a degradation area depends on the relative flux of the other ion that is being replaced. For

559   the degradation process near the cathode, the high relative flux of OH^- suggests a fast accumulation of SO_4^{2-} at an

560   early degradation stage, whilst the increased relative flux of SO_4^{2-} indicates an accelerated migration rate towards

561   the inner part of the specimen (Fig. 14a). In contrast, for the degradation process near the anode, the smaller

562   relative flux of Ca^{2+} than that of OH^- suggests a slower accumulation rate of the cations (Mg^{2+} or Na^+) than the

563   outflow of OH^- (Fig. 14b and 14c), which coincides with the shallow depth of Mg^{2+} and Na^+ incorporation (Fig. 5

564   and 10). The strengths of Na^+ and Mg^{2+} in the pore solution (Fig. 13d and 13f) and thus their relative fluxes (Fig.

565   14b and 14c) were different after the chemical reactions. As a result, Na^+ and Mg^{2+} showed different migration

566   behaviors (also compare Fig. 3 and Fig. 8). The different migration behaviors of SO_4^{2-} and Mg^{2+} were once realized

567   when using thermodynamic modeling to study the magnesium sulfate attack simply caused by diffusion [15,16]. It

568   was reported that the penetration depth of Mg^{2+} is usually overestimated compared to that of SO_4^{2-}. According to

569   the findings in this paper, this can be explained by the low concentration of Mg^{2+} in the pore solution and thus its

570   slower diffusion rate than SO_4^{2-}.

571

572   The electric migration of the cations and anions can also influence each other because both processes carry electric

573   charges. The experiment was conducted under a constant electric current. The same amount of charges should pass

574   through the specimen during the same period of time, no matter the specimen was exposed to $MgSO_4$ or Na_2SO_4. In

575   the cathode side, SO_4^{2-} was migrated from the cathodic solution into the cement paste. It penetrated through the

576   specimen together with OH^- (and other anions) in the pore solution. In the meanwhile, the Ca^{2+} in the pore solution

577   were released into the cathodic solution, but this process carried less electric charges due to the low relative flux of

578   Ca^{2+} than the anions. In the anode side exposed to $MgSO_4$, the migration of Mg^{2+} and Ca^{2+} towards the inner part of

579   the specimen were at low rates. The electric charges were mainly carried by the OH^- migrating from the inner part

580   of the specimen towards the anode side, and finally into the anodic solution. In contrast, in the case of Na_2SO_4

581   exposure, Na^+ could penetrate through the specimen much more easily than Mg^{2+}, and its electric migration can

582   carry much more electric charges. Under such circumstance, the electric migration of anions (SO_4^{2-} and OH^-) will

583   carry fewer charges, and thus the sulfate ingress will proceed on a lower rate compared with the situation of $MgSO_4$

584   exposure. Similar results were also reported in [41] but no convincing explanations were ever given.

585

586   *4.3 Comparison with the sulfate attack induced by diffusion*

587

588   To compare with the sulfate attack in the absence of electric field (induced by diffusion), the main mineralogical

589   alterations of Portland cement (Type I with limestone addition) mortars under Na_2SO_4 and $MgSO_4$ attacks [11,15]

590   and the results obtained in this paper are summarized in Table 3. This section focuses on the sulfate ingress and

591   decalcification near the cathode because a) these effects influenced a much wider area than the phase alterations

592   near the anode and b) similar processes also occur in the diffusion-induced sulfate attacks.

593

594   In the diffusion-induced Na_2SO_4 attack, the ingress of sulfate leads to the formation of ettringite followed by that of

595   gypsum. In the $MgSO_4$ attack, nevertheless, Mg^{2+} reacts with OH^- in the pore solution to form brucite, reducing the

596 solution pH to ~10.5 and inducing the decomposition of ettringite [60,61]. The decomposition of ettringite was also

597 observed here when the specimen is exposed to $MgSO_4$. This phenomenon can be also attributed to a reduction of

598 the pore solution alkalinity, but the presence of Mg^{2+} may not be a decisive factor considering the shallow depth of

599 the Mg transportation (Fig. 3b). During the sulfate ingress, the OH^- in the pore solution near the cathode was

600 theoretically transported towards the inner part of the specimen by the electric field. This process is used as a basic

601 assumption in the thermodynamic modeling and it is shown that the decomposition of ettringite and the formation

602 of gypsum occurred simultaneously with the decrease of OH^- concentration in the pore solution (Fig. 13b).

603 According to the test results, the presence of $CaSO_4$ in the cement paste near the cathode (Fig. 7) indicates

604 sufficient ionic strengths of Ca^{2+} and SO_4^{2-} for the stabilization of ettringite [2,14,15], whilst the Al content in the

605 hydration products did not show any apparent reduction (Fig. 3). It can be thus inferred that the decomposition of

606 ettringite was most probably caused by a neutralization process as assumed in the thermodynamic modeling. A

607 similar neutralization process was also observed when accelerating thaumasite sulfate attacks by applied electric

608 fields, and this process was also believed to destabilize ettringite according to [62].

609

610 **Table 3** Mineralogical alterations of sulfate attacks induced by electric migration (this paper) and diffusion
611 (obtained from [11,15]).

Process	Formation phase	Decomposition phase
Electric migration, cathode	Ettringite → Gypsum + Si-Al gel	Monocarbonate → Portlandite → Ettringite → C-S-H
Electric migration, anode, Na_2SO_4 [1]	Na-rich silica gel + Gypsum (surface)	Not clearly observed in the experiments
Electric migration, anode, $MgSO_4$ [1]	M-S-H + Brucite + Gypsum (surface)	Not clearly observed in the experiments
Diffusion, Na_2SO_4	Ettringite → Gypsum [2]	Monocarbonate → Portlandite → C-S-H
Diffusion, $MgSO_4$	Ettringite → Brucite → Gypsum → M-S-H	Monocarbonate → Portlandite → Ettringite → C-S-H

612 [1] Only the experimentally verified phases are listed in the formation column. The decomposition order of the hydration products was
613 not clearly observed in the experiments and thus is not listed in the decomposition column.

614 [2] Gypsum forms when the Na_2SO_4 concentration is high, e.g., 44 g/L in [11].

615

616 In the diffusion-induced sulfate attack, decalcification usually occurs on the surface of a specimen and is

617 characterized by the decomposition of portlandite and the decrease of the Ca/Si in C-S-H [1,63,64]. In the presence

618 of bicarbonate, gypsum will be the only stable sulfate-bearing product in the decalcification zone, and amorphous

619 SiO_2 and AH_3 are predicted as the stable phases by thermodynamic calculation [14,15]. Similar results are also

620 obtained in this paper (e.g., the $MgSO_4$ exposure for 28 d), but a different mechanism can be proposed when the

621 decalcification is induced by electric migration. According to the thermodynamic modeling, the relative flux of

622 Ca^{2+} migrating from the cement paste to the external solution accelerated during the degradation process (Fig. 14a).

623 This suggests that the loss of Ca^{2+} in the cement paste near the cathode cannot be fully compensated by the Ca^{2+}

624 migrating from the inner part of the specimen. The Ca^{2+} content near the cathode decreased (Fig. 3 and 8), thus

625 leading to the decalcification and the decomposition of hydration products. The decalcification near the cathode

626 may also have accelerated the transportation of Mg^{2+} through diffusion (Fig. 3b and Fig. 4c), as also reported in

627 concrete exposed to field conditions [65,66]. But the presence of Mg is not likely to be the cause of decalcification

628 here considering the depths of these processes (Fig. 4, Area III showed decalcification but very small Mg content).

629

630 The Ca/Si ratio (cf. Fig. 3 and Fig. 8) and portlandite content (cf. Fig. 7 and Fig. 12) indicate that the specimen

631 exposed to $MgSO_4$ had a higher degree of decalcification than that exposed to Na_2SO_4. On one hand, the

632 decalcification process is induced by the electric migration of Ca^{2+}. It will be impacted by the electric migration of

633 other cations (Mg^{2+} and Na^+), and thus the degree of decalcification coincides with that of sulfate ingress. On the

634 other hand, this process is also impacted by alterations of ionic strength in the external sulfate solution near the

635 cathode, which is a potential drawback of the test setup. When the specimen was exposed to Na_2SO_4, H^+ in the

636 solution would be reduced to H_2 on the cathode, thus producing OH^- in the solution [40] (Fig. 1b). Both OH^- and

637 SO_4^{2-} could carry electric charges and would migrate into the cement paste near the cathode. The OH^- migrating

638 towards the specimen may react with the Ca^{2+} that was driven out of the paste to form a surface layer consisting of

639   portlandite. When the Na_2SO_4 solution was refreshed (every 3 d), the portlandite might carbonate, forming a calcite

640   layer as observed in the SEM (Fig. 9). This hypothesis explains the slight increase of the Ca content near the

641   cathode area in Fig. 8b and a better protection from carbonation may help with its verification. In contrast, in the

642    $MgSO_4$ solution, the OH^- produced on the cathode precipitated with Mg^{2+} to form brucite in the external solution

643   (section 3.1.2). Owing to the precipitation of OH^-, SO_4^{2-} was the main anion migrating into the specimen, and thus

644    $CaSO_4$ formed on the surface of the specimen instead of calcite (Fig. 4b).

645

646   *4.4 Comparison with coupled reactive-transport modeling*

647

648   As stated in [1], the coupled reactive-transport modeling and the pure thermodynamic modeling presented

649   comparable results in revealing the phase alterations of a diffusion-induced sulfate attack. The pure thermodynamic

650   modeling is usually easy to use and provides fast results, but the results do not correspond directly with the real

651   exposure time or the depth from the exposure surface. In comparison, coupled reactive-transport modeling provides

652   the information of time and depth, but the accuracy depends strongly on the preciseness of models (e.g.,

653   transportation equation, fluid transport, charge balance) [21,67] and parameters (e.g., diffusion coefficient) [1]. This

654   paper proposed a simplified approach for the pure thermodynamic modeling study of electric-migration-induced

655   sulfate attacks. Such an approach focuses on the chemical and mineralogical aspects and clarifies alterations of the

656   hydration products. Although the real distribution of the products was not presented, this information can be

657   reflected by the relative flux that is proposed here. The advantages and validity of this approach will be further

658   demonstrated in an upcoming paper investigating the effect of supplementary cementitious materials in the same

659   situation.

660

661   The thermodynamic modeling calculation conducted in this paper is based on the assumption that the kinetics of the

662   chemical reactions is much faster than the transportation of ionic species, and that the hydration system is close to

663   an equilibrium state. As reviewed in [68], this assumption is usually valid in most practical cases involving the

664   diffusion of ions in saturated systems, and thus it is widely accepted by the existing pure thermodynamic modeling

665   studies [1,2,11,14-16]. In contrast, electric migration usually induces a quicker ionic motion, and thus the

666   equilibrium state is more difficult to be reached [24]. When studying the electric migration of chloride by coupled

667   reactive-transport models, an equilibrium state was assumed in [69] and the test results agree well with the

668   modeling. The results of this paper also show that the migration behavior of ionic species coincides with the

669   solution chemistry (relative flux) under the assumption of equilibrium. It can be thus inferred that the real solution

670   chemistry in the hydrated cement paste is similar to that under the equilibrium state and that the equilibrium

671   assumption is likely to be valid in the case of electric migration.

672

673   The electric migration behavior of ionic species can be represented by the relative flux, which depends on the ion's

674   diffusion coefficient and concentration in the pore solution. The diffusion coefficients of different ions are usually

675   at the same order of magnitude, as shown in Table 2. However, their concentrations can span several orders of

676   magnitude, which induces wide differences in the relative fluxes and is responsible for the different migration

677   behavior of Mg^{2+}, Na^{+}, and SO_4^{2-} under applied electric fields. In this respect, for a reactive-transport process, it is

678   sometimes acceptable to suppose the same diffusion coefficient for different ionic species, as was done in

679   [16,70,71]. Nevertheless, the effect of chemical reactions on the concentration and thus the migration of ionic

680   species should be carefully considered.

681

682   *4.5 Comparison with real-life situations*

683

This setup simulates both processes when electric current flows into and out of the cement-based materials simultaneously. In contrast, in the case of DC stray current, these two processes occur separately. The electric current enters the concrete at a certain location, goes through the reinforcement, and then flows out of the concrete at another location [29]. The ionic exchange between the external environment and cement-based materials induced by the inflow and outflow of electric current can be represented by the anode area and cathode area in this setup, respectively, but the behavior of the reinforcements, e.g., anodic corrosion or hydrogen evolution, is not simulated. Moreover, this paper focused on the chemical and mineralogical aspects of sulfate attacks and thus the physical and microstructural aspects, including expansion and cracking, were not investigated. During the electric migration tests, the specimens did not show significant cracking, which agrees with the focus of this paper but may possibly differ from the real situation. The test results (Fig. 7) and thermodynamic modeling (Fig. 13a) both indicate the decomposition of ettringite at the late degradation stage, probably suggesting the absence of expansion at that stage. However, thermodynamic modeling predicted an increased volume of hydration products near the cathode, which may yet cause expansion. Based on the results of this paper, it is difficult to determine whether expansion and cracking will occur under such circumstances.

698

The concentration of ions in the external solution will change with time, and this will be the other difference between the test setup and the real-life situation. Although the concentration of the sulfate solution theoretically remains above ~0.34 mol/L due to the 3-day periodically refreshment (see section 2.2 and Supplementary Data), it seems that the alterations of the ionic strength in the external sulfate solution have still impact the products formed on the surface of the specimens (see section 4.3). Increasing the volume of the external solutions and shortening the refreshing cycle can be solutions to this problem.

705

The test setup used here has been proposed for the purpose of laboratory acceleration tests [39-41]. The discussion

in section 4.3 demonstrates that the electric migration of ionic species near the cathode not only induce the ingress

of sulfate, but also cause a neutralization process in the pore solution and a decalcification process (see also Table

3). These effects should be considered when interpreting the mineralogical alterations obtained by such test setups,

especially when a) $MgSO_4$ attack is investigated and the degradation proceeds to the late-stage quickly and b) a

long exposure time is investigated in the case of Na_2SO_4 attack and the degradation may proceed to a later stage

compared with that in this paper. After an exposure time of 28 d, SO_4^{2-} from the cathodic solution had penetrated

through most of the specimen and even influenced the area that is 5–10 mm deep from the anode, as indicated by

the distribution of hydration products (Fig. 7 and Fig. 12). Specimens with greater height are thus recommended for

such tests, especially in the case of long duration (e.g., > 28 d exposure time), in order that the real penetration

depth of SO_4^{2-} can be accurately identified from an uncontaminated area.

717

In addition to the situations mentioned above, we believe that the simplified approach for the thermodynamic

modeling study proposed in this paper can be more broadly applied in investigating the behavior of cement-based

materials under applied electric fields. Future studies may involve the use of this approach in accelerated

electrochemical leaching tests [37,38], other types of chemical attacks, and in concrete technologies involving

electrochemical methods (e.g., chloride extraction, realkalinization, and electrochemical deposit [32-34]).

723

5 Conclusions

725

When an electric current flows out of a Portland cement paste (in the cathode area of the specimen), the electric

727   migration of ionic species induced the ingress of sulfate from the external solution. Ettringite formed at the initial

728   stage but decomposed to form gypsum at a later stage. Thermodynamic modeling indicates that the alkalinity of the

729   pore solution decreased during this process, which is most probably responsible for the decomposition of ettringite.

730   In addition to the sulfate ingress, decalcification also occurred in this area, which is characterized by the

731   decomposition of portlandite followed by that of C-S-H. When the specimen was exposed to $MgSO_4$, the sulfate

732   ingress and decalcification proceeded to a later stage and occurred in a deeper area compared with the specimen

733   exposed to Na_2SO_4.

734

735   Near the anode, electric current flows into the cement paste, and the electric charges were mainly carried by the

736   electric migration of OH^- from the pore solution towards the external solution. The Ca^{2+} originally in the pore

737   solution migrated towards the inner part of the specimen at a much lower rate than that of OH^-, and thus the

738   incorporation of the cations from the external solution (Mg^{2+} or Na^+) was slow. The incorporation of Mg^{2+} formed

739   brucite and M-S-H–like products. Thermodynamic modeling indicates that this process induced a low Mg^{2+}

740   concentration in the pore solution, and thus Mg^{2+} would not effectively migrate into the inner part of the specimen.

741   In contrast, the incorporation of Na^+ formed Na-rich silica gel, during which the Na^+ concentration in the pore

742   solution was much higher. As a result, Na^+ showed a better capability of migration and can penetrate through the

743   cement paste easily. Since both cations and anions can carry electric charges, the different migration behaviors of

744   Mg^{2+} and Na^+ are attributed to inducing the different degrees of sulfate ingress near the cathode.

745

746   A simplified approach based on thermodynamic modeling and the ionic transportation equation were newly

747   proposed to provide insights into the degradation processes of the sulfate attacks that are induced by electric

748   migration. In addition to calculating the degradation phase assemblage, the migration behavior of ionic species

749 under electric fields can be represented by the relative flux. We believe this approach can be more broadly applied

750 to predict the behavior of cement-based materials under electric fields.

751

752 **Acknowledgements**

753

757

758 **Appendix A. Supplementary Data**

759

760 1 Estimating the concentration range of the sulfate solution

761 2 Rietveld refinement

762 3 Input recipes for thermodynamic modeling

763 4 Mineralogical alterations of cement paste tested by TGA

764

765 **References**

766

767 [1] B. Lothenbach, B. Bary, P. Le Bescop, T. Schmidt, N. Leterrier, Sulfate ingress in Portland cement, Cem. Concr. Res.

768 40 (2010) 1211-1225.

769 [2] W. Kunther, B. Lothenbach, K.L. Scrivener, On the relevance of volume increase for the length changes of mortar

770 bars in sulfate solutions, Cem. Concr. Res. 46 (2013) 23-29.

771   [3] M. Whittaker, L. Black, Current knowledge of external sulfate attack, Adv. Cem. Res. 27 (2015) 532-545.

772   [4] R.J. Flatt, G.W. Scherer, Thermodynamics of crystallization stresses in DEF, Cem. Concr. Res. 38 (2008) 325-336.

773   [5] R. Flatt, N. Aly Mohamed, F. Caruso, H. Derluyn, J. Desarnaud, B. Lubelli, R.M. Espinosa-Marzal, L. Pel, C.

774   Rodriguez-Navarro, G.W. Scherer, N. Shahidzadeh, M. Steiger, Predicting salt damage in practice: A theoretical insight

775   into laboratory tests, RILEM Technical Letters. 2 (2017) 108.

776   [6] W. Müllauer, R.E. Beddoe, D. Heinz, Sulfate attack expansion mechanisms, Cem. Concr. Res. 52 (2013) 208-215.

777   [7] C. Yu, W. Sun, K. Scrivener, Mechanism of expansion of mortars immersed in sodium sulfate solutions, Cem. Concr.

778   Res. 43 (2013) 105-111.

779   [8] C. Yu, W. Sun, K. Scrivener, Degradation mechanism of slag blended mortars immersed in sodium sulfate solution,

780   Cem. Concr. Res. 72 (2015) 37-47.

781   [9] M. Santhanam, M.D. Cohen, J. Olek, Effects of gypsum formation on the performance of cement mortars during

782   external sulfate attack, Cem. Concr. Res. 33 (2003) 325-332.

783   [10] B. Tian, M.D. Cohen, Does gypsum formation during sulfate attack on concrete lead to expansion?, Cem. Concr.

784   Res. 30 (2000) 117-123.

785   [11] T. Schmidt, B. Lothenbach, M. Romer, J. Neuenschwander, K. Scrivener, Physical and microstructural aspects of

786   sulfate attack on ordinary and limestone blended Portland cements, Cem. Concr. Res. 39 (2009) 1111-1121.

787   [12] B. Bary, N. Leterrier, E. Deville, P. Le Bescop, Coupled chemo-transport-mechanical modelling and numerical

788   simulation of external sulfate attack in mortar, Cem. Concr. Compos. 49 (2014) 70-83.

789   [13] A. Soive, V.Q. Tran, External sulfate attack of cementitious materials: New insights gained through numerical

790   modeling including dissolution/precipitation kinetics and surface complexation, Cem. Concr. Compos. 83 (2017)

791   263-272.

792   [14] W. Kunther, B. Lothenbach, K. Scrivener, Influence of bicarbonate ions on the deterioration of mortar bars in sulfate

793   solutions, Cem. Concr. Res. 44 (2013) 77-86.

794   [15] W. Kunther, B. Lothenbach, Improved volume stability of mortar bars exposed to magnesium sulfate in the presence

795   of bicarbonate ions, Cem. Concr. Res. 109 (2018) 217-229.

796   [16] W. Kunther, B. Lothenbach, K.L. Scrivener, Deterioration of mortar bars immersed in magnesium containing sulfate

797   solutions, Mater. Struct. 46 (2013) 2003-2011.

798   [17] Z. Makhloufi, S. Aggoun, B. Benabed, E.H. Kadri, M.Bederina, Effect of magnesium sulfate on the durability of

799   limestone mortars based on quaternary blended cements, Cem. Concr. Compos. 65 (2016) 186-199.

800   [18] B. Huber, H. Hilbig, J.E. Drewes, E. Müller, Evaluation of concrete corrosion after short- and long-term exposure to

801   chemically and microbially generated sulfuric acid, Cem. Concr. Res. 94 (2017) 36-48.

802   [19] L. Gu, P. Visintin, T. Bennett, Evaluation of accelerated degradation test methods for cementitious composites

803   subject to sulfuric acid attack; application to conventional and alkali-activated concretes, Cem. Concr. Compos. 87 (2018)

804   187-204.

805   [20] E. Rozière, A. Loukili, R. El Hachem, F. Grondin, Durability of concrete exposed to leaching and external sulphate

806   attacks, Cem. Concr. Res. 39 (2009) 1188-1198.

807   [21] E. Samson, J. Marchand, Modeling the transport of ions in unsaturated cement-based materials, Computers &

808   Structures. 85 (2007) 1740-1756.

809   [22] R.A. Patel, Q.T. Phung, S.C. Seetharam, J. Perko, D. Jacques, N. Maes, G. De Schutter, G. Ye, K. Van Breugel,

810   Diffusivity of saturated ordinary Portland cement-based materials: A critical review of experimental and analytical

811   modelling approaches, Cem. Concr. Res. 90 (2016) 52-72.

812   [23] P. Yang, G. Sant, N. Neithalath, A refined, self-consistent Poisson-Nernst-Planck (PNP) model for electrically

813   induced transport of multiple ionic species through concrete, Cem. Concr. Compos. 82 (2017) 80-94.

814   [24] E. Samson, J. Marchand, K.A. Snyder, Calculation of ionic diffusion coefficients on the basis of migration test

815   results, Mater. Struct. 36 (2003) 156-165.

816   [25] J.M. Galíndez, J. Molinero, On the relevance of electrochemical diffusion for the modeling of degradation of

817   cementitious materials, Cem. Concr. Compos. 32 (2010) 351-359.

818   [26] C. Li, M. Wu, W. Yao, Effect of coupled B/Na and B/Ba doping on hydraulic properties of belite-ye'elimite-ferrite

819   cement, Constr. Build. Mater. 208 (2019) 23-35.

820   [27] L. Bertolini, M. Carsana, P. Pedeferri, Corrosion behaviour of steel in concrete in the presence of stray current,

821   Corros. Sci. 49 (2007) 1056-1068.

822   [28] A. Aghajani, M. Urgen, L. Bertolini, Effects of DC stray current on concrete permeability, J. Mater. Civ. Eng. 28

823   (2015) 04015177.

824   [29] A. Solgaard, M. Carsana, M. Geiker, A. Küter, L. Bertolini, Experimental observations of stray current effects on

825   steel fibres embedded in mortar, Corros. Sci. 74 (2013) 1-12.

826   [30] F. Wittmann, Corrosion of cement-based materials under the influence of an electric field, Mater. Sci. Forum,

827   Trans Tech Publ, 1997, pp. 107-126.

828   [31] G. Glass, N. Buenfeld, The inhibitive effects of electrochemical treatment applied to steel in concrete, Corros. Sci.

829   42 (2000) 923-927.

830   [32] W.H.A. Peelen, R.B. Polder, E. Redaelli, L. Bertolini, Qualitative model of concrete acidification due to cathodic

831   protection, Mater. Corros. 59 (2008) 81-89.

832   [33] Y. Chen, W. Yao, J. Zuo, Effect of ultrasound on electrochemical chloride extraction from mortar, Materials

833   Research Express. 5 (2018) 036508.

834   [34] W. Li, B. Dong, Z. Yang, J. Xu, Q. Chen, H. Li, F. Xing, Z. Jiang, Recent Advances in Intrinsic Self-Healing

835   Cementitious Materials, Adv. Mater. 30 (2018) e1705679.

836   [35] J. García, F. Almeraya, C. Barrios, C. Gaona, R. Núñez, I. López, M. Rodríguez, A. Martínez-Villafañe, J.M.

837 Bastidas, Effect of cathodic protection on steel–concrete bond strength using ion migration measurements, Cem. Concr.

838 Compos. 34 (2012) 242-247.

839 [36] J.C. Orellan, G. Escadeillas, G. Arliguie, Electrochemical chloride extraction: efficiency and side effects, Cem.

840 Concr. Res. 34 (2004) 227-234.

841 [37] A. Babaahmadi, L. Tang, Z. Abbas, T. Zack, P. Mårtensson, Development of an electro-chemical accelerated ageing

842 method for leaching of calcium from cementitious materials, Mater. Struct. 49 (2016) 705-718.

843 [38] A. Babaahmadi, L. Tang, Z. Abbas, P. Mårtensson, Physical and Mechanical Properties of Cementitious Specimens

844 Exposed to an Electrochemically Derived Accelerated Leaching of Calcium, International Journal of Concrete Structures

845 and Materials. 9 (2015) 295-306.

846 [39] Q. Huang, C. Wang, C. Yang, L. Zhou, J. Yin, Accelerated sulfate attack on mortars using electrical pulse, Constr.

847 Build. Mater. 95 (2015) 875-881.

848 [40] Q. Huang, C. Wang, C. Luo, C. Yang, Y. Luo, H. Xie, Effect of mineral admixtures on sulfate resistance of mortars

849 under electrical field, Adv. Cem. Res. 29 (2017) 45-53.

850 [41] S. Lorente, M.-P. Yssorche-Cubaynes, J. Auger, Sulfate transfer through concrete: Migration and diffusion results,

851 Cem. Concr. Compos. 33 (2011) 735-741.

852 [42] A. Susanto, D.A. Koleva, O. Copuroglu, K. van Beek, K. van Breugel, Mechanical, electrical and microstructural

853 properties of cement-based materials in conditions of stray current flow, Journal of Advanced Concrete Technology. 11

854 (2013) 119-134.

855 [43] K. Scrivener, R. Snellings, B. Lothenbach, A practical guide to microstructural analysis of cementitious materials,

856 Crc Press, 2016.

857 [44] W. Dollase, Correction of intensities for preferred orientation in powder diffractometry: application of the March

858 model, J. Appl. Crystallogr. 19 (1986) 267-272.

859   [45] R. Snellings, A. Bazzoni, K. Scrivener, The existence of amorphous phase in Portland cements: Physical factors

860   affecting Rietveld quantitative phase analysis, Cem. Concr. Res. 59 (2014) 139-146.

861   [46] M.A.G. Aranda, A.G. De la Torre, L. Leon-Reina, Rietveld Quantitative Phase Analysis of OPC Clinkers, Cements

862   and Hydration Products, Reviews in Mineralogy and Geochemistry. 74 (2012) 169-209.

863   [47] K. Mohan, H. Taylor, Analytical Electron Microscopy of Cement Pastes: IV, β-Dicalcium Silicate Pastes, J. Am.

864   Ceram. Soc. 64 (1981) 717-719.

865   [48] J. Li, G. Geng, R. Myers, Y.-S. Yu, D. Shapiro, C. Carraro, R. Maboudian, P.J.M. Monteiro, The chemistry and

866   structure of calcium (alumino) silicate hydrate: A study by XANES, ptychographic imaging, and wide- and small-angle

867   scattering, Cem. Concr. Res. 115 (2019) 367-378.

868   [49] J. Kerr, D. Lide, CRC Handbook of Chemistry and Physics, CRC Press Boca Raton, FL, USA, 2000.

869   [50] J. Xia, L.-y. Li, Numerical simulation of ionic transport in cement paste under the action of externally applied

870   electric field, Constr. Build. Mater. 39 (2013) 51-59.

871   [51] C. Andrade, R. Buják, Effects of some mineral additions to Portland cement on reinforcement corrosion, Cem. Concr.

872   Res. 53 (2013) 59-67.

873   [52] D.A. Kulik, T. Wagner, S.V. Dmytrieva, G. Kosakowski, F.F. Hingerl, K.V. Chudnenko, U.R. Berner, GEM-Selektor

874   geochemical modeling package: revised algorithm and GEMS3K numerical kernel for coupled simulation codes,

875   Computational Geosciences. 17 (2013) 1-24.

876   [53] W. Hummel, U. Berner, E. Curti, F. Pearson, T. Thoenen, Nagra/PSI chemical thermodynamic data base 01/01,

877   Radiochimica Acta. 90 (2002) 805-813.

878   [54] B. Lothenbach, D.A. Kulik, T. Matschei, M. Balonis, L. Baquerizo, B. Dilnesa, G.D. Miron, R.J. Myers, Cemdata18:

879   A chemical thermodynamic database for hydrated Portland cements and alkali-activated materials, Cem. Concr. Res. 115

880   (2019) 472-506.

881   [55] B.Z. Dilnesa, B. Lothenbach, G. Renaudin, A. Wichser, D. Kulik, Synthesis and characterization of hydrogarnet

882    $Ca_3(Al_xFe_{1-x})_2(SiO_4)_y(OH)_{4(3-y)}$, Cem. Concr. Res. 59 (2014) 96-111.

883   [56] C. Li, M. Wu, W. Yao, Eco-efficient Cementitious System Consisting of Belite-Ye'elimite-Ferrite Cement,

884   Limestone Filler, and Silica Fume, ACS Sustainable Chem. Eng. 7 (2019) 7941-7950.

885   [57] Q. Zeng, C. Wang, Y. Luo, C. Yu, Q. Huang, C. Luo, Effect of temperatures on TSA in cement mortars under

886   electrical field, Constr. Build. Mater. 162 (2018) 88-95.

887   [58] B. Lothenbach, G. Le Saout, E. Gallucci, K. Scrivener, Influence of limestone on the hydration of Portland cements,

888   Cem. Concr. Res. 38 (2008) 848-860.

889   [59] M. Vespa, B. Lothenbach, R. Dähn, T. Huthwelker, E. Wieland, Characterisation of magnesium silicate hydrate

890   phases (M-S-H): A combined approach using synchrotron-based absorption-spectroscopy and ab initio calculations, Cem.

891   Concr. Res. 109 (2018) 175-183.

892   [60] O.S.B. Al-Amoudi, Attack on plain and blended cements exposed to aggressive sulfate environments, Cem. Concr.

893   Compos. 24 (2002) 305-316.

894   [61] P. Brown, S. Badger, The distributions of bound sulfates and chlorides in concrete subjected to mixed NaCl, $MgSO_4$,

895   Na_2SO_4 attack, Cem. Concr. Res. 30 (2000) 1535-1542.

896   [62] Y. Luo, C. Wang, Z. Fang, L. Xiao, Q. Zeng, The TSA degradation process of cement-based materials in the

897   electrical field environment, Constr. Build. Mater. 206 (2019) 703-716.

898   [63] R. Gollop, H. Taylor, Microstructural and microanalytical studies of sulfate attack. IV. Reactions of a slag cement

899   paste with sodium and magnesium sulfate solutions, Cem. Concr. Res. 26 (1996) 1013-1028.

900   [64] W. Kunther, B. Lothenbach, J. Skibsted, Influence of the Ca/Si ratio of the C–S–H phase on the interaction with

901   sulfate ions and its impact on the ettringite crystallization pressure, Cem. Concr. Res. 69 (2015) 37-49.

902   [65] C. Li, M. Wu, Q. Chen, Z. Jiang, Chemical and mineralogical alterations of concrete subjected to chemical attacks in

903   complex underground tunnel environments during 20–36 years, Cem. Concr. Compos. 86 (2018) 139-159.

904   [66] M. Rosenqvist, A. Bertron, K. Fridh, M. Hassanzadeh, Concrete alteration due to 55 years of exposure to river water:

905   Chemical and mineralogical characterisation, Cem. Concr. Res. 92 (2017) 110-120.

906   [67] E. Samson, J. Marchand, K.A. Snyder, J. Beaudoin, Modeling ion and fluid transport in unsaturated cement systems

907   in isothermal conditions, Cem. Concr. Res. 35 (2005) 141-153.

908   [68] E. Samson, J. Marchand, J. Beaudoin, Modeling the influence of chemical reactions on the mechanisms of ionic

909   transport in porous materials: an overview, Cem. Concr. Res. 30 (2000) 1895-1902.

910   [69] D. Conciatori, É. Grégoire, É. Samson, J. Marchand, L. Chouinard, Statistical analysis of concrete transport

911   properties, Mater. Struct. 47 (2013) 89-103.

912   [70] E. Stora, B. Bary, Q.C. He, E. Deville, P. Montarnal, Modelling and simulations of the chemo–mechanical behaviour

913   of leached cement-based materials: leaching process and induced loss of stiffness, Cem. Concr. Res. 39 (2009) 763-772.

914   [71] E. Stora, B. Bary, Q.C. He, E. Deville, P. Montarnal, Modelling and simulations of the chemo-mechanical behaviour

915   of leached cement-based materials: Interactions between damage and leaching, Cem. Concr. Res. 40 (2010) 1226-1236.

916